
1 **Chemical properties, sources and size-resolved**
2 **hygroscopicity of submicron black carbon-containing**
3 **aerosols in urban Shanghai**

4 Shijie Cui¹, Dan Dan Huang², Yangzhou Wu^{1,a}, Junfeng Wang¹, Fuzhen Shen^{1,b}, Jiukun
5 Xian¹, Yunjiang Zhang¹, Hongli Wang², Cheng Huang², Hong Liao¹, Xinlei Ge^{1,*}

6
7 ¹ Jiangsu Key Laboratory of Atmospheric Environment Monitoring and Pollution
8 Control, Collaborative Innovation Center of Atmospheric Environment and Equipment
9 Technology, School of Environmental Science and Engineering, Nanjing University of
10 Information Science and Technology, Nanjing 210044, China

11 ² Shanghai Academy of Environmental Sciences, Shanghai 200233, China

12 ^anow at: Department of Atmospheric Sciences, School of Earth Sciences, Zhejiang
13 University, Hangzhou 310027, PR China

14 ^bnow at: Department of Meteorology, University of Reading, Reading, RG6 6BX, UK

15
16 *Corresponding author: Xinlei Ge (Email: caxinra@163.com)

17
18 *For Atmospheric Chemistry and Physics*
19

20 **Abstract.** Refractory black carbon (*r*BC) aerosols play an important role in air quality
21 and climate change, yet high time-resolved and detailed investigation on the
22 physicochemical properties of *r*BC and its associated coating is still scarce. In this work,
23 we used a laser-only Aerodyne soot particle aerosol mass spectrometer (SP-AMS) to
24 exclusively measure the *r*BC-containing (*r*BCc) particles, and compared their
25 properties with the total non-refractory submicron particles (NR-PM₁) measured in
26 parallel by a high-resolution AMS (HR-AMS) in Shanghai. The observation shows that
27 *r*BC was overall thickly coated with an average mass ratio of coating to *r*BC core (R_{BC})
28 of ~ 5.0 (± 1.7). However, mass of *r*BC coating species only occupied 19.1% (± 4.9)%
29 of those in NR-PM₁; sulfate tended to condense preferentially on non-*r*BC particles
30 therefore its portion on *r*BC was only 7.4% (± 2.2)%, while the majority of primary
31 organic aerosols (POA) were associated with *r*BC (72.7 ± 21.0 %). Positive matrix
32 factorization reveals that cooking emitted organics did not coat on *r*BC, and a portion
33 of organics coated on *r*BC was from biomass burning which was unidentifiable in NR-
34 PM₁-organics. Small *r*BCc particles were predominantly from traffic, while large-sized
35 ones were often mixed with secondary components and typically had thick coating.
36 ~~During this campaign, sulfate~~Sulfate and secondary organic aerosol (SOA) species
37 were generated mainly through daytime photochemical oxidation (SOA formation
38 likely involved with in-situ chemical conversion of traffic-related POA to SOA), while
39 nocturnal heterogeneous formation was dominant for nitrate; we also estimated the
40 average times of 5~19 hours for those secondary species to coat on *r*BC. Particles
41 during a short period that was affected by ship emissions, were characterized with a
42 high vanadium concentration (on average $5.86.3 \pm 3.1$ ng m⁻³) and a mean
43 vanadium/nickel mass ratio of 2.0 (± 0.6). Furthermore, the size-resolved
44 hygroscopicity parameter (κ_{rBCc}) of *r*BCc particles was obtained based on its fully
45 chemical characterization, and was parameterized as $\kappa_{rBCc}(x) = 0.29 - 0.14 \times \exp(-0.006$
46 $\times x)$ (x is from 150 to 1000 nm). Under critical supersaturations (SS_C) of 0.1% and 0.2%,
47 the D_{50} values were 166 (± 16) and 110 (± 5) nm, respectively, and with 16 (± 3)%
48 and 59 (± 4)% of *r*BCc in number could be activated into cloud condensation nuclei
49 (CCN). Our findings are valuable to advance the understanding of BC chemistry as well

50 as the effective control of atmospheric BC pollution.

51 **1 Introduction**

52 Refractory black carbon (*r*BC) aerosols can directly absorb solar radiation,
53 indirectly change the nature of cloud and alter the albedo of snow or glaciers (~~Jacobi et~~
54 ~~al., 2015~~)(Jacobi et al., 2015), resulting in a positive radiative forcing that is second
55 only to carbon dioxide on both regional and global scales (Ramanathan and Carmichael,
56 2008;Bond et al., 2013). The fresh *r*BC particles produced by incomplete combustion
57 of biomass and fossil fuel tend to be fractal in morphology and can mix with many other
58 components (Peng et al., 2016;Li et al., 2021). After entering into the atmosphere, fresh
59 *r*BC can further externally or internally mix with organic/inorganic species which are
60 primarily emitted or secondarily formed, and such aged *r*BC-containing (*r*BCc)
61 particles (Chen et al., 2017;Lee et al., 2017) might have contrasting chemical properties
62 and morphologies (or mixing states) (Liu et al., 2017a;Lee et al., 2019;Xie et al., 2019).
63 In addition, when *r*BC mixes with hydrophilic materials, its hygroscopicity, cloud
64 condensation nuclei (CCN) activity and size distribution, etc., can be significantly
65 changed, which subsequently affect its atmospheric behavior, impact and lifecycle (~~Liu~~
66 ~~et al., 2013;Lambe et al., 2015~~)(Liu et al., 2013;Lambe et al., 2015). Therefore, it is
67 necessary to elucidate the physicochemical characteristics and sources of *r*BC cores
68 and associated coating materials, so as to better understand their influences on climate
69 and air quality.

70 Chemical composition of ambient *r*BCc particles is largely dependent upon
71 atmospheric conditions and emission sources. In general, the thickness of coating, mass
72 contribution of secondary components (such as sulfate, nitrate and secondary organic
73 aerosol (SOA) species) and oxidation degree of the coated organics of *r*BCc particles,
74 increase with the aging time or oxidation capacity of ambient environment (Cappa et
75 al., 2012;Liu et al., 2015;Wang et al., 2017;Collier et al., 2018;Wang et al., 2019),
76 except in some specific cases that thickly coated *r*BCc might be dominated by primarily
77 emitted particles (such as from biomass burning (Wang et al., 2017)). Recent field
78 observations report that SOA species coated on *r*BC cores could account for 35% and
79 41% of the total SOA mass near traffic emission sources and in a polluted offshore

80 environment, respectively (Massoli et al., 2012;Massoli et al., 2015). A study of *rBCc*
81 particles in Singapore finds that over 90% of *rBC* derived from local combustion
82 sources (mainly traffic), while 30% of *rBC* was associated with fresh SOA generated
83 under the influences of daytime shipping and industrial emissions (~~Rivellini et al.,~~
84 ~~2020~~)(Rivellini et al., 2020). The SOA material concentrated on the surface of *rBC* was
85 found to be chemically different from the SOA that was externally mixed with *rBC*
86 (~~Lee et al., 2017~~)(Lee et al., 2017) in Fontana, California, and another study in
87 Shenzhen, China, reveals that more oxidized SOA preferred to mix with *rBC* due to
88 that abundant transition metals detected on *rBC* cores might act as catalysts to convert
89 less oxidized SOA to more oxidized SOA in aerosol aqueous phase (~~Cao et al.,~~
90 ~~2022~~)(Cao et al., 2022); the *rBC* could catalyze SO₂ to form sulfate as well, as observed
91 in Beijing (~~Zhang et al., 2020~~)(Zhang et al., 2020) and Guangzhou (~~Zhang et al.,~~
92 ~~2021~~)(Zhang et al., 2021), China. Besides SOA, cooking-related OA is found to be
93 externally mixed with *rBC* (Lee et al., 2017;Wang et al., 2019), and a unique biomass
94 burning related OA factor was identified and was only present in *rBCc* rather than non-
95 *rBC* particles during summertime in Beijing (Wang et al., 2020a).

域代码已更改

96 Size distribution of *rBCc* particles is also modulated greatly by their original
97 sources and ageing processes. For example, a study in Shanghai shows a bimodal size
98 distribution of *rBCc*, with a condensation mode dominated by traffic emissions (small
99 core size, thin coating) and a droplet mode including highly aged biomass burning
100 particles (large core size and thick coating) and highly aged traffic particles (small core
101 size and very thick coating) (~~Gong et al., 2016~~)(Gong et al., 2016). Another study in
102 Beijing (~~Liu et al., 2019~~)(Liu et al., 2019) further resolves four size modes of *rBCc*,
103 relevant with traffic (small core, thin coating), coal or biomass burning (moderate
104 coating, both small and large cores), coal combustion (large core, think coating) and
105 secondary process (thick coating, both small and large cores).

106 Moreover, water uptake and CCN activity of *rBCc* particles can increase with the
107 encapsulation of water-soluble substances such as sulfate, nitrate, and SOA (Liu et al.,
108 2013;Wu et al., 2019). Based on the measured chemical composition of *rBCc*, our
109 previous work has established a method for calculating size-resolved hygroscopicity

110 parameters of $rBCc$ (κ_{rBCc}), and determined the CCN activation diameters of $rBCc$
111 particles for given critical supersaturation (SS_C) values (Wu et al., 2019).

112 Highly time-resolved chemical characterization of $rBCc$ particles were seldom
113 reported in China and is still lacking in Shanghai. In this study, we utilized an Aerodyne
114 soot particle aerosol mass spectrometer (SP-AMS) to determine the concentration,
115 composition and size distribution of $rBCc$ particles exclusively (technical details in
116 Section 2.1) in urban Shanghai for the first time. We also compared the SP-AMS
117 measurement results with those from a co-located Aerodyne high-resolution time-of-
118 flight aerosol mass spectrometer (HR-AMS), to comprehensively investigate the
119 characteristics of $rBCc$ particles. We analyzed κ_{rBCc} and estimated the proportions of
120 activated $rBCc$ numbers at given SS_C as well.

121

122 **2 Experimental methods**

123 **2.1 Sampling site and instrumentation**

124 The field measurement was conducted from October 31 to December 2, 2018,
125 during which the instruments were deployed on 8th floor of the building of Shanghai
126 Academy of Environmental Sciences (SAES) (31°10'33.348" N, 121°26'10.978" E).
127 Shanghai can be a representative of the densely populated megacity across the world;
128 the measurement period also belonged to the cold season when sources of $rBCc$ might
129 be complex, and can offer rich information about the $rBCc$; of course, future
130 measurements in other seasons are still essential to achieve a complete understanding
131 of $rBCc$. East of the sampling site is a large commercial shopping center, and the site
132 is surrounded by residential areas with two busy arterial roads directly to the east (~450
133 m) and south (~150 m), respectively (Figure S1 in the supporting information). In
134 addition, the adjacent areas are densely populated with roadside residents, office
135 workers, and market traders, as well as crowds in and out of the Caobao Road Metro
136 station (~100 m). The measurement period was dominated by northeasterly winds,
137 while many international freight companies located on northeastern side of the site, and
138 many freighters were reposing on the Huangpu River. Overall, the sampling site was
139 probably influenced by vehicular emissions, residential activities and the northeast

140 Cargo ship emission plumes, etc.

141 An Aerodyne SP-AMS and an HR-AMS were operated in parallel during the
142 campaign. The two AMSs shared a same sampling line with a PM_{2.5} cyclone (Model
143 URG-2000-30EN) in front to remove coarse particles. Ambient air pulled through the
144 sampling line was dried using a diffusion dryer filled with silicon gel and was
145 subsequently drawn into both instruments. Due to the transmission efficiency of the
146 inlet lens, both AMSs measured mainly particles of 30-1200 nm (denoted as PM₁).

147 The working principle of SP-AMS has been described in detail previously (~~Onasch~~
148 ~~et al., 2012~~)(Onasch et al., 2012). However, in this work, we used only the intracavity
149 infrared laser vaporizer to selectively measure *r*BCc particles (*r*BC cores and associated
150 coating materials), as *r*BC can absorb 1064 nm laser light. The thermal tungsten
151 vaporizer had to be physically detached otherwise non-*r*BC particles can still be
152 detected as the filament can heat the vaporizer to ~200 °C even if it was turned off.
153 Before sampling, the SP-AMS was tuned and calibrated following the steps described
154 previously (Lee et al., 2015; Willis et al., 2016; Wang et al., 2017). During sampling, due
155 to relatively low *r*BCc mass loadings, the SP-AMS was operated with two mass
156 sensitive V modes (2.5 minutes per cycle), one with a particle time-of-flight (PToF)
157 mode (30 s) and another one (120 s) with a mass spectral mode with mass-to-charge
158 (*m/z*) ratio up to 500. Filtered air was also measured in the middle of campaign (for 60
159 min) to determine the limits of detection (LOD, three times the standard deviation) of
160 various aerosol species and to adjust the air-influenced mass spectral signals (~~Zhang et~~
161 ~~al., 2005~~)(Zhang et al., 2005).

162 Before removal of the tungsten heater, the calibrations of ionization efficiency (IE)
163 for nitrate and relative ionization efficiency (RIE) of sulfate were performed by using
164 pure ammonium nitrate and ammonium sulfate particles (~~Jayne et al., 2000~~)(Jayne et
165 ~~al., 2000~~), and the values were assumed to be unchanged throughout the whole
166 campaign (~~Willis et al., 2016~~)(Willis et al., 2016). RIE of *r*BC to nitrate was calibrated
167 by using size-selected (300 nm) BC particles (REGAL 400R pigment black, Cabot
168 Corp.) (~~Onasch et al., 2012~~)(Onasch et al., 2012), and the average ratio of C₁⁺ to C₃⁺
169 was calculated to be 0.584 to correct the interference on C₁⁺ from other organics. RIEs

170 of ammonium, nitrate, sulfate and *r*BC were determined to be 4.53, 1.10, 1.01, and 0.17,
171 respectively, and RIE of organics used the default value of 1.4 (Canagaratna et al., 2007).
172 The size was calibrated by Polystyrene latex (PSL) spheres (100–700 nm) (Duke
173 Scientific Corp., Palo Alto, CA) before the measurement. This study applied a
174 collection efficiency (CE) of 0.5 for SP-AMS.

175 ~~The co-located HR-AMS (DeCarlo et al., 2006)~~The co-located HR-AMS
176 (DeCarlo et al., 2006) was used to measure all PM₁ including both *r*BCc and non-*r*BC
177 particles, but it detected only non-refractory species (NR-PM₁ species) as its 600 °C
178 thermal heater is unable to vaporize *r*BC and other refractory components. In addition,
179 mass concentrations of gaseous pollutants, carbon monoxide (CO), ozone (O₃),
180 nitrogen dioxide (NO₂), and sulfur dioxide (SO₂) were measured by the Thermo
181 Scientific analyzers provided by SAES. Meteorological parameters including air
182 temperature (T), relative humidity (RH), wind speed (WS), wind direction (WD) and
183 precipitation, were obtained from Xujiahui Environmental Monitoring Station of
184 Shanghai (31°11'49.1424"N, 121°26'34.44" E)(~2400 m away from the site). The
185 concentrations of particle-phase vanadium (V) and nickel (Ni) that were used to
186 investigate ship influence were measured independently by an Atmospheric heavy
187 metal analyzer (XHAM-2000A, SAIL HERO., China).

188

189 2.2 Data analysis

190 The AMS data (both SP-AMS and HR-AMS) were analyzed using standard ToF-
191 AMS data analysis tool (Squirrel version 1.59D and Pika version 1.19D), based on Igor
192 Pro 6.37 (Wavemetrics, Lake Oswego, OR, USA). The mass concentrations and high
193 resolution mass spectra (HRMS) of *r*BC and coating species (*r*BC_{CT}) were calculated
194 from high-resolution (HR) fitting of V-mode data. Size distributions of *r*BCc
195 components were determined by the PToF data with unit mass resolution and were
196 scaled to their mass concentrations obtained above. In particular, size distribution of
197 *r*BC was scaled to that of *m/z* 24 (C₂⁺) (the scaling factor is *r*BC mass concentration to
198 that of calculated based on its size distribution), because *m/z* 24 as a *r*BC fragment, has
199 least interference from other organic or inorganic species; such treatment was adopted

200 in earlier studies too (Collier et al., 2018; Wang et al., 2019; Wang et al., 2016).

201 The HR ion fitting of AMS data is able to distinguish various ions and isotopic
202 ions and calculate elemental ratios of organics such as oxygen-to-carbon (O/C),
203 hydrogen-to-carbon (H/C), nitrogen-to-carbon (N/C), and organic mass to organic
204 carbon (OM/OC) ratios, via the original Aiken-ambient (A-A) method (Aiken et al.,
205 2008) and the improved method (I-A) (Canagaratna et al., 2015b). Outcomes of both
206 methods correlated well. Average O/C, H/C, and OM/OC ratios from the I-A method
207 used in this work were 24.9%, 7.3%, and 5.6%, respectively, higher than those from the
208 A-A method.

209 Furthermore, we performed Positive matrix factorization (PMF) (Paatero and
210 Tapper, 1994)(Paatero and Tapper, 1994) analysis on the HRMS of organics measured
211 by the SP-AMS via the PMF Evaluation Tool (Ulbrich et al., 2009)(Ulbrich et al., 2009).
212 The PMF solutions were thoroughly evaluated following the protocols documented in
213 Zhang et al. (2011)Zhang et al. (2011). Finally, a 6-factor solution was chosen as the
214 optimal one. The final result included four primary OA (POA) factors, namely
215 hydrocarbon-like species enriched OA (HOA-rich), *r*BC-enriched OA (*r*BC-rich),
216 biomass burning OA (BBOA), water-soluble hydrocarbon-like species enriched OA
217 (WS-HOA), and two secondary OA (SOA) factors including a less oxidized oxygenated
218 OA (LO-OOA_{*r*BC}), and a more oxidized oxygenated OA (MO-OOA_{*r*BC}) (Key diagnostic
219 plots in Fig. S2). As a comparison, the mass spectra of 5-factor and 7-factor solutions
220 are illustrated in Fig. S3 (for the 5-factor solution, factor 3 is a mixed factor of BBOA
221 and WS-HOA, while for the 7-factor solution, MO-OOA clearly splits into factor 5 and
222 factor 2). The HR-AMS data were processed in a similar way, and four factors of NR-
223 PM₁ organics were resolved, including hydrocarbon-related OA (HOA_{NR-PM1}), cooking
224 OA (COA_{NR-PM1}), less oxidized oxygenated OA (LO-OOA_{NR-PM1}), and more oxidized
225 oxygenated OA (MO-OOA_{NR-PM1}) (Mass spectra and time series shown in Fig. S3S4).
226

227 2.3 Calculation of size-resolved hygroscopicity of *r*BCc

228 The hygroscopicity parameter κ is a single parameter representing the
229 hygroscopicity of particles, calculated based on essentially the chemical composition

230 ~~(Petters and Kreidenweis, 2007)~~(Petters and Kreidenweis, 2007). SP-AMS measured
231 size-resolved chemical compositions of $rBCc$ can thus lead to size-resolved
232 hygroscopicity of $rBCc$ (κ_{rBCc}) (Wu et al., 2019;Hu et al., 2021). This study applied a
233 similar method proposed by Wu et al. (2019) and the critical parameters involved in
234 calculation are detailed in Table S1. The procedures are briefly described here: (1)
235 obtain the matrix of size-resolved mass concentrations of each $rBCc$ component from
236 SP-AMS analysis; (2) convert the size-resolved concentration matrix of inorganic ions
237 (SO_4^{2-} , NO_3^- and NH_4^+) to corresponding matrix of inorganic salts (NH_4NO_3 , NH_4HSO_4 ,
238 $(NH_4)_2SO_4$) using a simplified solution of ion pairs ~~(Gysel et al., 2007)~~(Gysel et al.,
239 2007); (3) convert the size-resolved mass matrix of all components (inorganic salts,
240 OA and rBC) to those of size-resolved volume fractions (Gysel et al., 2007;Chang et
241 al., 2010;Wu et al., 2016); (4) combine with previously reported hygroscopic
242 parameters (Gysel et al., 2007;Chang et al., 2010;Wu et al., 2016) to obtain the
243 volumetric contributions of each component to the hygroscopicity of $rBCc$; (5) use the
244 Zdanovskii-Stokes-Robinson (ZSR) rule to derive the size-resolved hygroscopicity of
245 $rBCc$ (κ_{rBCc}) (Topping et al., 2005a, b2005b, a).

246

247 **3 Results and discussion**

248 **3.1 Overview of chemical characteristics of $rBCc$ and NR-PM₁ particles**

249 Figure 1 presents the time series of meteorological parameters, concentrations of
250 gaseous pollutants (CO , NO_2 , O_3 , and SO_2), ship emission tracers (vanadium and
251 nickel), rBC and rBC_{CT} species and their mass percentages to the total $rBCc$ mass,
252 PMF-resolved OA factors and their corresponding fractional contributions. The
253 sampling period was featured by relatively moderate temperatures and very stagnant
254 conditions with average ($\pm 1\sigma$) temperature of $15.3 \pm (\pm 2.9)^\circ C$ and wind speed (WS)
255 of $0.16 \pm (\pm 0.29) m s^{-1}$. ~~Calm~~The wind (~~with speeds $< 0.5 m s^{-1}$~~) dominated most of
256 the sampling days and 42% of sampling time was with near-zero wind, therefore overall
257 influence of WS and WD on surface mass loadings of $rBCc$ was insignificant. Yet one
258 should keep in mind that WD can affect $rBCc$ sources, and WS in higher altitude might
259 be stronger therefore long-range transport of air pollutants was still possible. The

260 average concentrations of CO, NO₂, O₃, SO₂, V, and Ni were determined to be 0.60 (\pm
261 0.26) ppm, 29.20 (\pm 17.07) ppt, 27.10 (\pm 15.97) ppt, 1.27 (\pm 0.72) ppt, 4.05 (\pm 3.19)
262 ng m⁻³, and 3.06 (\pm 2.45) ng m⁻³, respectively.

263 The mass loadings of *r*BC and *r*BC_{CT} ranged from 0.04 to 11.00 μg m⁻³ and 0.37
264 to 30.47 μg m⁻³ with campaign-mean values (\pm 1σ) of 0.92 ~~\pm (\pm 0.81)~~ μg m⁻³ and 4.55
265 ~~\pm (\pm 4.40)~~ μg m⁻³. The coating materials accounted for ~~83.0%~~ 81.8 (\pm 5.3)% of the total
266 *r*BC_C mass, of which organics was the most abundant species (2.54 \pm 2.52 μg m⁻³,
267 46.96 \pm 6.4%), followed by nitrate (1.20 \pm 1.30 μg m⁻³, ~~20~~ 18.5 \pm 8.0%), ammonium
268 (0.44 \pm 0.40 μg m⁻³, 98.0 \pm 2.0%), sulfate (0.30 \pm 0.19 μg m⁻³, 7.1 \pm 3.6-0%), and
269 chloride (0.07 \pm 0.05 μg m⁻³, 1.7 \pm 1.0%). The mass ratio of *r*BC_{CT} to *r*BC (*R*_{BC}) ranged
270 from 2.2 to 9.0, with an average of \sim 5.0 (\pm 1.7). The average *R*_{BC} was higher than that
271 in California (*R*_{BC}=2.3) (~~Collier et al., 2018~~)(Collier et al., 2018) and in Shenzhen (*R*_{BC}
272 = 2.5)(~~Cao et al., 2022~~)(Cao et al., 2022), lower than that in Tibetan Plateau (*R*_{BC}=7.7)
273 (Wang et al., 2017) and similar to that in Beijing (*R*_{BC}=5.0) (~~Wang et al., 2019~~)(Wang
274 et al., 2019), suggesting *r*BC was relatively thickly coated throughout the campaign.
275 Correlation between *r*BC and *r*BC_{CT} was moderate (Pearson's $r^2 = r =$ 0.5876).
276 Correlation coefficients (r^2) of chloride, nitrate, sulfate and organics with *r*BC were
277 0.5272, 0.7587, 0.5471 and 0.5373, respectively, suggesting variability of sources
278 among different coating components.

279 Figure 2 compares the campaign-averaged diurnal patterns of *r*BC_C and NR-PM₁
280 species, chemical compositions of *r*BC_C and NR-PM₁, and mass ratios of the species
281 coated on *r*BC to those of NR-PM₁. We found that the diurnal variations of nitrate,
282 sulfate, ammonium, chloride were very similar ($r^2 > r >$ 0.8692) between the two particle
283 groups, while apparent difference was found for *r*BC_C organics with a much obvious
284 morning rush hour peak (6:00 - 9:00). The results indicate that the formation processes
285 of inorganic salts coated on *r*BC were similar to those uncoated on *r*BC, but there were
286 large difference regarding sources/processes existed for organics. For *r*BC itself, the
287 diurnal cycle presented clearly a morning peak and an evening peak, likely relevant
288 with rush hour traffic emissions (CO showed similar pattern). On the contrary, *R*_{BC} had
289 a minimum in the morning and dropped to a low level in later afternoon, probably due

290 to influence from traffic-emitted fresh and barely coated *r*BC particles (details in
291 Section 3.2.1).

292 Distributions of species between *r*BCc and non-*r*BC particles were also different,
293 leading to different chemical compositions (Figs. 2g and 2h). Sulfate tended to
294 preferentially condense on non-*r*BC particles, as its mass contribution to total *r*BCc
295 mass was only 6.5%, ($\pm 4.2\%$), while its contribution to total NR-PM₁ was 17.6%. (\pm
296 8.3%). Apportionment of nitrate between *r*BCc and non-*r*BC particles was about even
297 as it both occupied ~26% of the total *r*BCc and NR-PM₁ masses. Organics occupied
298 55.9% ($\pm 9.2\%$) of *r*BCc mass, larger than it in NR-PM₁ ($43.7 \pm 11.7\%$), due to that
299 primary OA species preferentially associated with *r*BC. Such result is similar to that
300 observed in winter in Beijing but contrary to the result that SOA was more abundant in
301 *r*BCc in Shenzhen (Cao et al., 2022)(Cao et al., 2022).

302 On average, *r*BC_C accounted for 19.1% of the total NR-PM₁ mass loading (21.61
303 $\pm 15.80 \mu\text{g m}^{-3}$)(Fig. 2i), comparable to that in Fontana, California (Lee et al.,
304 2017)(Lee et al., 2017). The finding reveals that significant fractions of aerosol species
305 were externally mixed with *r*BC. Individually, sulfate captured by *r*BC only represented
306 7.4% ($\pm 2.2\%$) of NR-PM₁ sulfate, similar to the earlier results (Lee et al.,
307 2017; Wang et al., 2020a; Cao et al., 2022; Ma et al., 2020); mass fractions of *r*BCc
308 nitrate ($20.1 \pm 5.2\%$) and chloride ($20.4 \pm 5.5\%$) in NR-PM₁ were similar to the portion
309 of total *r*BC_C ($19.1 \pm 4.9\%$), while the fraction of organics was higher (26.1%). ($\pm 7.3\%$).
310 The lower fraction of sulfate in *r*BCc than nitrate was likely due to a few reasons. One
311 probable reason is traffic was a dominant source of *r*BC (see Section 3.2.1 for details)
312 and NO₂ is known to be mainly from traffic as well, therefore secondarily formed nitrate
313 was easy to condense on co-emitted *r*BC, however SO₂ is mainly from other sources
314 rather than traffic. Another possible cause is that *r*BC concentration was relatively high
315 during nighttime, and nighttime formation of nitrate was significant; Sulfate, on the
316 other hand, was mostly formed in the afternoon due to photochemical oxidation in this
317 study (see Section 3.3.2 for details), whereas afternoon *r*BC concentration was low.

318 The relatively high ratio of organics was attributed to the fact that majority of POA
319 species were coated on *r*BC (average ratio of $72.7 \pm 21.0\%$), while *r*BC-related SOA

带格式的

320 was 21.8% ($\pm 7.7\%$) of the total. Note the *r*BCc POA here included all four POA factors,
321 and COA_{NR-PM1} did not coat on *r*BC thus was not included in the calculation.

322

323 **3.2 Distinctive sources of OA in *r*BCc and in NR-PM₁**

324 As shown previously, source apportionment results of OA in *r*BCc and NR-PM₁
325 were different. This section discusses in details the characteristics of OA sources in
326 *r*BCc and in bulk NR-PM₁.

327 **3.2.1 Source apportionment of OA in *r*BCc**

328 Figure 3 shows the HRMS and temporal variations of the six OA factors resolved
329 from PMF analysis of *r*BCc organics. Note the PMF analysis included *r*BC signals (i.e.,
330 C_x⁺ ions) to aid identification of different factors, yet calculations of elemental ratios of
331 these OA factors did not include C_x⁺ ions in order to explicitly explore the properties of
332 organic coating. The HRMS of HOA-rich and *r*BC-rich were similar to the OA
333 previously reported in urban environments near traffic emissions and/or in
334 gasoline/diesel vehicle exhaust (Massoli et al., 2012; Lee et al., 2015; Enroth et al.,
335 2016; Saarikoski et al., 2016; Willis et al., 2016; Lee et al., 2017), therefore both factors
336 were traffic-related. The HOA-rich mass spectrum was featured by intense hydrocarbon
337 ion series (i.e., C_nH_{2n+1}⁺ and C_nH_{2n-1}⁺ ions in Fig. 3c), and a lowest O/C ratio of 0.07.
338 Mass fraction of *r*BC signals (i.e., C_n⁺ ions, such as *m/z* 12, 24, 36, 48, and 60, etc.) in
339 HOA-rich was 8.1%. Mass spectrum of *r*BC-rich factor had remarkable contribution
340 from *r*BC (24.2%). Beside C_n⁺ ions, the *r*BC-rich factor contained more oxygenated
341 organic fragments and presented a higher O/C ratio of 0.21 than that of HOA-rich,
342 similar to previous studies (Willis et al., 2016; Lee et al., 2017). This result is reasonable
343 as previous studies (Corbin et al., 2014; Malmberg et al., 2017) found that refractory
344 organics could generate oxygenated ion fragments (such as CO⁺ and CO₂⁺ derived from
345 oxygenated species on soot surface or inside soot nanostructure). HOA-rich factor
346 correlated very well with the common AMS tracer of vehicular OA, C₄H₉⁺ (*r*=0.95, Fig.
347 3i), while *r*BC-rich factor did match the variation of *r*BC well (*r*=0.90, Fig. 3g). Since
348 diesel combustion often releases more *r*BC than that of gasoline, it is likely that the
349 *r*BC-rich factor is representative of diesel vehicle exhaust while HOA-rich factor

350 represents gasoline combustion emissions. This result demonstrates that laser-only SP-
351 AMS is capable of distinguishing diesel and gasoline burning particles which typically
352 cannot be separated by other AMS measurements. Further verification should be subject
353 of future work.

354 In this work, a multiple linear regression for the three-dimension size-resolved
355 mass spectra according to the method provided in Ulbrich et al. (2012) was used to
356 resolve the average size distributions of six OA factors. The diagnostic plots are shown
357 in Fig. 4. Overall, the lumped size distribution of six OA factor could reproduce well
358 that of total OA (except for a few size bins, most deviations are within 10%).
359 Correlation between measured and reconstructed OA of all size bins was very tight with
360 r of 0.99 and a slope of 0.97, indicating the robustness of the regressed size distributions
361 of all OA factors. The results together with size distributions of r BCc components, and
362 corresponding mass fractional contributions of different components in all size bins are
363 illustrated in Fig. 5. The average HOA-rich size distribution peaked around 150 nm
364 (D_{va} , vacuum aerodynamic diameter), generally matching with previously reported size
365 distribution of HOA (Sun et al., 2012;Ulbrich et al., 2012;Zhou et al., 2016).
366 Interestingly, size distribution of r BC-rich factor presented two modes, with one
367 peaking \sim 260 nm, and a more pronounced one peaking \sim 580 nm (Fig. 5a).

368 The BBOA was identified owing to its obviously higher signals of $C_2H_4O_2^+$ (2.03%)
369 and $C_3H_5O_2^+$ (1.62%) than those in other factors, as these two ions are well-known AMS
370 fragments of the biomass burning tracer, levoglucosan (Mohr et al., 2009;Cubison et
371 al., 2011). ~~In addition, the~~The time series of BBOA correlated particularly tightly with
372 both marker ions (r of 0.86 and 0.80, respectively); it in fact also correlated well with
373 K^+ ($r=0.79$), another tracer of biomass burning emission. The O/C and H/C ratios of
374 BBOA were 0.12 and 1.78, and C_n^+ ions accounted for 9.1% of BBOA, all suggesting
375 that the factor was fresh and might be co-emitted with r BC. A relatively high N/C ratio
376 (0.033) was found for BBOA, which could be attributed to the large amounts of
377 nitrogen-containing organic species enriched in biomass burning OA (~~Laskin et al.,~~
378 ~~2009~~)(Laskin et al., 2009). In addition, the size distribution of BBOA (Fig. 5a) (peak
379 size \sim 500 nm) was similar to that of biomass burning BC-containing particles obtained

380 using single particle mass spectrometry in Shanghai ([Gong et al., 2016](#))([Gong et al.,](#)
381 [2016](#)).

382 The PMF analysis deconvoluted a unique OA factor coated on *r*BC, namely WS-
383 HOA. Firstly, the WS-HOA mass spectrum had a series of hydrocarbon ion fragments
384 and its time series correlated well with them (e.g., *r* of 0.90 and 0.92 for WS-HOA vs.
385 $C_4H_7^+$ and $C_4H_9^+$, respectively). Secondly, this factor correlated the best (*r*=0.57) with
386 aerosol liquid water content (ALWC) (Fig. 3j) compared with the other five OA factors
387 (all *r*<0.2). ~~Thirdly, a previous study (Ye et al., 2017)~~Thirdly, a previous study ([Ye et](#)
388 [al., 2017](#)) that investigated specially the water-soluble fraction of OA via PMF analysis,
389 separated also a HOA factor that contained significant nitrogen-containing organic
390 fragments, with a highest N/C ratio among all other factors, and correlated well those
391 nitrogenated fragments. The WS-HOA defined here showed similar characteristics with
392 the highest N/C (0.037) among all factors and tight correlations with nitrogen-
393 containing fragments (*r*>0.80). At last, although WS-HOA had a relatively high O/C
394 (0.31) with remarkable contributions from $C_2H_3O^+$ and CO_2^+ , yet its correlations with
395 these two ions were in fact not strong (*r* of 0.46 and 0.44, respectively); and WS-HOA
396 had the least fraction of *r*BC fragments (0.9%) (note *r*BC is hydrophobic), even less
397 than the two SOAs (Fig. 3d). Both results suggest that this factor is a collection of
398 water-soluble primary OA species. The peak of WS-HOA size distribution was ~150
399 nm, close to that of HOA-rich (Figs. 5a). ~~Aqueous-phase processed SOA (aqSOA) were~~
400 ~~typically with very high O/C ratio (Xu et al., 2019)~~Aqueous-phase processed SOA
401 ~~(aqSOA) were typically with very high O/C ratio (Xu et al., 2019)~~, and size distribution
402 of aqSOA often presented a droplet mode, peaking in relatively large sizes (such as
403 500~600 nm)([Gilardoni et al., 2016](#);[Wang et al., 2021](#);[Ge et al., 2012](#)). Therefore, the
404 moderate O/C (0.31) and small mode size of WS-HOA again manifest it was not from
405 aqueous-phase reactions but more likely the water-soluble fraction of POA.

406 The PMF analyses separated two SOA factors, LO-OOA_{*r*BC} and MO-OOA_{*r*BC}.
407 Mass spectral features of the two SOAs were consistent with previous studies: The LO-
408 OOA_{*r*BC} was rich in $C_xH_yO_1^+$ ions (38.7%) (such as $C_2H_3O^+$ at *m/z* 43) but with less
409 contribution from $C_xH_yO_2^+$ ions (7.6%) and an overall moderate O/C (0.25), while MO-

410 OOA_{rBC} had much more contribution from C_xH_yO₂⁺ ion family (22.7%) (such as CO₂⁺
411 at *m/z* 44) and C_xH_yO₁⁺ ions (44.7%), with a high O/C ratio (0.56). In addition, LO-
412 OOA_{rBC} correlated better with nitrate (*r*=0.83) than it with sulfate (*r*=0.69), while the
413 correlation between MO-OOA_{rBC} and sulfate (*r*=0.84) is better than it with nitrate
414 (*r*=0.76). Size distributions of the two SOAs were also in accord with their secondary
415 behaviors, both accumulating at larger sizes (~450 nm for LO-OOA_{rBC}, and a bit larger
416 mode size of ~500 nm for MO-OOA_{rBC}), in agreement with previous observations (Sun
417 et al., 2012;Ulbrich et al., 2012;Zhou et al., 2016).

418 In total, traffic-related POA (sum of HOA-rich, *r*BC-rich and WS-HOA) was the
419 most abundant source of *r*BCc organics (39.1%); BBOA occupied ~18.4%; the
420 contributions of two SOAs were on par with each other (20.2% for LO-OOA_{rBC}, and
421 22.3% for MO-OOA_{rBC}) (Fig. 2g). Among traffic POA, gasoline derived HOA-rich
422 factor outweighed the diesel derived *r*BC-rich factor (11.4% vs. 6.3% of the total *r*BCc).
423 Contributions of different factors varied greatly for different sizes of *r*BCc particles
424 (Fig. 5b). Small-sized particles were overwhelmingly dominated by traffic POA; SOA
425 contributions increased with increase of size, and dominated over POA for 300-800 nm
426 ones; contribution of BBOA was also relative larger for 300-800 nm than for other-
427 sized ones; the very large particles (800-1000 nm) were found to be affected mainly by
428 traffic POA in this work. Correspondingly, for the total *r*BCc particles, *r*BC cores
429 peaked at ~170 nm, while other secondary inorganic components, behaving like SOA
430 factors, all peaked at a big size (~550 nm) (Fig. 5c) and their mass percentages were
431 also large for large-sized particles (Fig. 5d).

432 Figure 6a further demonstrates the changes of mass fractions of each *r*BCc
433 component as a function of *R*_{BC}. *R*_{BC} is a proxy of coating thickness. It was found that
434 the thinly coated *r*BCc (*R*_{BC}<3) were dominated (up to ~80%) by traffic-related POA.
435 With the increase of *R*_{BC}, contribution of secondary components increased gradually,
436 especially the two SOAs and nitrate (sulfate showed little changes across the whole *R*_{BC}
437 range); SOA and nitrate contributions reached 40.2% and 31.3% at *R*_{BC} = 8, respectively.
438 Accordingly, the oxidation degree (OSc = 2*O/C-H/C) (Kroll et al., 2011)(Kroll et al.,
439 2011) of coated organics increased with *R*_{BC}. In Fig. 6b, we presented the mass

440 contributions of OA factors to the r BC mass at different R_{BC} values. The r BC was as
441 expected, predominantly associated with POA (from 94% at $R_{BC}<2$ to 66% at $R_{BC}>8$),
442 similar to those from Fontana (Lee et al., 2017). Contribution of r BC-rich factor
443 decreased obviously, and those of SOA factors increased with R_{BC} . The contributions
444 of HOA-rich, WS-HOA and BBOA factors changed little.

445

446 3.2.2 Comparisons with NR-PM₁ organics

447 As shown in Fig. S3S4, PMF analysis separated four OA factor for NR-PM₁
448 organics. Two SOA factors (LO-OOA and MO-OOA) were resolved for both r BCc and
449 NR-PM₁, and their contributions to them were also close (Figs. 2g and 2h). Correlations
450 of time series between the two LO-OOA factors and between the two MO-OOA factors
451 were also tight (r of 0.94 and 0.90, respectively), indicating similar formation processes
452 for each SOA. But, of course, the SOAs from r BCc and from NR-PM₁ were not entirely
453 the same, as later ones had higher O/C ratios (0.52 of LO-OOA_{NR-PM1} and 0.62 of MO-
454 OOA_{NR-PM1}). On average, the portion of LO-OOA coated on r BC took up 21.6% mass
455 of LO-OOA in total NR-PM₁, and the portion was 26.0% for MO-OOA. This result
456 suggests that there were some ~~but not big~~ differences regarding the partitioning of LO-
457 OOA and MO-OOA onto r BCc and non- r BC particles.

458 Compared with SOAs, source apportionment results of POA were quite distinct.
459 Firstly, there was only one HOA factor resolved for NR-PM₁, while three HOA factors
460 were separated for r BCc. Note the r BC-rich and WS-HOA factors occupied merely
461 3.1% and 2.1% of NR-PM₁ OA mass, respectively, probably the cause that they were
462 not identified in NR-PM₁ OA. Nevertheless, mass loadings of the sum of HOA-rich,
463 r BC-rich and WS-HOA factors (termed as HOA _{r BC}) agreed quite well with that of
464 HOA_{NR-PM1} ($r=0.95$) (Fig. 7a), verifying both source apportionment results. And,
465 HOA _{r BC} took up 63.7% of HOA_{NR-PM1}, while previous studies reported that 81%
466 ~~(Massoli et al., 2012) and 87% (Massoli et al., 2015) of HOA were associated with~~
467 ~~r BC. These results imply that HOA species in NR-PM₁ were largely internally mixed~~
468 ~~with r BC affected by vehicular emissions. Secondly, COA_{NR-PM1} was only identified in~~
469 ~~NR-PM₁ OA. AMS resolved COA_{NR-PM1} is mainly from cooking oil and food itself,~~

470 ~~therefore it negligibly internally mixes with rBC . This result is consistent with previous~~
471 ~~observations (Massoli et al., 2012) and 87 % (Massoli et al., 2015) of HOA were~~
472 ~~associated with rBC . These results imply that HOA species in NR-PM₁ were largely~~
473 ~~internally mixed with rBC affected by vehicular emissions. Secondly, COA_{NR-PM₁} was~~
474 ~~only identified in NR-PM₁ OA. AMS-resolved COA_{NR-PM₁} is mainly from cooking oil~~
475 ~~and food ingredients, therefore it negligibly internally mixes with rBC . This result is~~
476 ~~consistent with previous observations (Lee et al., 2015; Willis et al., 2016; Lee et al.,~~
477 ~~2017; Collier et al., 2018). At last, BBOA was identified in $rBCc$ OA but not in NR-PM₁~~
478 ~~OA. One plausible reason was that the BBOA mass contribution was minor (equivalent~~
479 ~~to <5% of NR-PM₁ OA mass); another speculation is that laser only SP-AMS can detect~~
480 ~~refractory species that HR-AMS cannot, some of them might be originated from~~
481 ~~biomass burning (Wang et al., 2020a). At last, BBOA was identified in $rBCc$ OA but~~
482 ~~not in NR-PM₁ OA. One plausible reason was that the BBOA mass contribution was~~
483 ~~minor (equivalent to <5% of NR-PM₁ OA mass) therefore was not able to be separated~~
484 ~~from other OA factors; another speculation is that laser only SP-AMS can detect~~
485 ~~refractory species that HR-AMS cannot, and a portion of these refractory species are~~
486 ~~likely rich in biomass burning OA. Identification of BBOA in $rBCc$ rather than in~~
487 ~~simultaneously measured total NR-PM₁ was also found in Tibet (Wang et al., 2017) and~~
488 ~~Beijing (Wang et al., 2020a), role of such BBOA and its interplay with rBC core remain~~
489 ~~a subject of future work.~~

490 Diurnal cycles of the POA and SOA factors from both PMF analyses are compared
491 in Figs. 7b and 7c. The diurnal pattern of stacked HOA _{rBC} indeed agreed with that of
492 HOA_{NR-PM₁}, both with two peaks in the morning and evening rush hours, and, the
493 patterns of rBC -rich, HOA-rich, and WS-HOA factors showed similar behaviors
494 individually (Fig. 7b). The diurnal variation of COA_{NR-PM₁} had pronounced peaks
495 during lunch and dinner times, and its percentage in NR-PM₁ OA reached 54% at night.
496 Diurnal patterns of two LO-OOA factors were somewhat different ($r=0.35$). LO-
497 OOA _{rBC} has a major peak in the afternoon, while though LO-OOA_{NR-PM₁} concentration
498 rose in the afternoon too but peaked in early evening (~8 pm 20:00). The daily variations
499 of two MO-OOA factors were similar ($r=0.83$), both peaking at 16:00. The afternoon

500 increases of both SOAs indicate an important role of photochemical reactions, yet
501 differences in formation mechanisms, volatilities and partitioning behaviors of SOA
502 products could lead to diversities of their diurnal patterns and HRMS.

503

504 **3.3 Evolution and formation *r*BCc components**

505 **3.3.1 Behaviors of *r*BC cores**

506 Size distribution of *r*BC cores shown in Fig. 5c was relatively wide. Beside the
507 main peak at ~170 nm, it extended significantly into large sizes and had a small peak at
508 ~550 nm, which was close to the peak of secondary components. With results shown in
509 Fig. 5a, we found that small *r*BC cores were often thinly coated, while thickly coated
510 *r*BCc particle were often highly aged and a portion of them also had large-sized *r*BC
511 cores. This result is likely owing to that oxidation of *r*BC-bounded organics and/or
512 condensation of secondary species onto *r*BC surface can induce restructuring of soot
513 aggregates to form compact and large cores (Chen et al., 2018; Chen et al., 2016). Such
514 phenomenon is in line with earlier studies (Liu et al., 2019; Gong et al., 2016). We
515 further show the image plot of size distributions of *r*BC at different R_{BC} in Fig. [S5a-S6a](#).
516 It can be found that the *r*BC mass in a large part concentrated in particles with R_{BC} of
517 5-8, and there was indeed a significant portion of *r*BC appearing in large size range
518 (400-800 nm) with very thick coating (R_{BC} of 8-9).

519

520 **3.3.2 Formation of inorganic salts**

521 Sulfate and nitrate both peaked at a big size ~550 nm (Fig. 5c) and were mainly
522 associated with thickly coated *r*BCc ($R_{BC}>6$, Figs. [S5d-S6d](#) and [S5e-S6e](#)). To investigate
523 the impacts of photochemistry and aqueous/heterogeneous chemistry on the formation
524 of *r*BC_{CT} species, we plotted the image plots of size distributions of nitrate, sulfate and
525 organics versus O_X ($O_3 + NO_2$) and relative humidity (RH) in Fig. 8. Here O_X is used
526 as a proxy of photochemical activity (Xu et al., 2017), and RH is an indicator of aqueous
527 reactions ([Wu et al., 2018](#))([Wu et al., 2018](#)). Nitrate significantly concentrated in 65-
528 100 ppb O_X range but there was a weak accumulation in low O_X as well (Fig. 8a), while
529 in Fig. 8d, nitrate had a prominent hotspot in $RH>85\%$. Generally, both strong

530 photochemical activity and high RH could promote nitrate formation. For sulfate,
531 although the distribution was scattered due to low level of mass loadings, high O_x level
532 seemed to favor sulfate formation (Fig. 8b); sulfate was scattered in the whole RH range
533 and there were some enhancements at high RH (>80%) but was much less clear-cut
534 (Fig. 8e). Therefore aqueous-phase production of sulfate was not important in this
535 campaign.

536 We further calculated the sulfur oxidation ratio (SOR) and nitrogen oxidation ratio
537 (NOR) (Xu et al., 2014)(Xu et al., 2014), and plotted their variations against O_x and
538 RH in Figs. 9a and 9e, respectively. The NOR rose substantially at O_x >60 ppb but
539 showed no increase at O_x < 60 ppb, while it increased continuously with RH. Mass ratio
540 of nitrate to rBC stayed at a high level during nighttime when RH was high as well
541 (overall diurnal trend of NO₃/rBC was similar to that of RH, see Figs. S6aS7a and
542 S6dS7d). This result indicates a likely more important role of nocturnal nitrate
543 formation (N₂O₅ hydrolysis) (Pathak et al., 2011)(Pathak et al., 2011) (Sun et al.,
544 2011)(Sun et al., 2011) than photochemical production of nitrate during this campaign;
545 moreover, low temperature and high RH favor nitrate partitioning into the particle phase
546 during nighttime too (Gao et al., 2011)(Gao et al., 2011). For sulfate, The SOR
547 increased with O_x while it increased with RH under relatively dry conditions (<60%)
548 but decreased with RH when RH>60%. This result, on the other hand, highlights that
549 photochemical production is more important than aqueous/heterogenous formation for
550 sulfate. In addition, mass ratios of sulfate to rBC were enhanced remarkably during
551 daytime and peaked in the afternoon (Fig. S6eS7e), supporting the key role of
552 photochemical formation of sulfate. Sulfate precursor SO₂ was at a high level during
553 daytime too. The main formation pathway of sulfate is strikingly different from that
554 observed in winter Nanjing (Wu et al., 2018)(Wu et al., 2018), suggesting significant
555 seasonal variability of sulfate formation even in the same region.

556

557 3.3.3 Evolution of organics

558 Organics had a broad average size distribution (Fig. 5c), but unlike rBC, its main
559 peak appeared at 500~600 nm. Figure S5bS6b shows that the majority of organics

560 partitioned in rBC with R_{BC} of 5.0-9.0 and wide size coverage (300-800 nm).
561 Regarding its dependences on O_X and RH, it mainly accumulated at $O_X > 70$ ppb (Fig.
562 8c) and very high RH (~90%) (Fig. 8f). Consistently, O/C ratio and OSc both peaked
563 in the afternoon (Fig. S6bS7b), all suggesting a critical role of photochemistry in
564 affecting the behavior of organics.

565 Figure 9 illustrates the mass ratios of each OA factor to rBC varying with O_X and
566 RH. Mass ratios of all four POA factors generally presented decreasing trends (despite
567 some fluctuations) against O_X (Fig. 9b), and the total POA_{rBC} showed evident decrease
568 with increase of O_X (Fig. 9d). Instead, both $LO-OOA_{rBC}$ and $MO-OOA_{rBC}$, as well as
569 their sum (SOA_{rBC}) increased continuously with O_X (Figs. 9c and 9d). This result proves
570 that photochemical oxidation contributed significantly to both $LO-OOA_{rBC}$ and $MO-$
571 OOA_{rBC} formations. Comparatively, decreases of POA_{rBC} perhaps point to its reaction
572 loss upon photochemical oxidation. With regard to RH, besides WS-HOA, the other
573 three POA_{rBC} factors showed almost no dependences on RH (Fig. 9f); note the increase
574 of WS-HOA with RH did not indicate the aqueous production of WS-HOA (see
575 discussion in Section 3.2.1), but a result of enhanced dissolution with increase of
576 moisture. Overall small increase of POA_{rBC} (Fig. 9h) with RH then mainly attributed to
577 WS-HOA. Contrary to the trends with O_X , mass ratios of two SOA factors as well as
578 the total SOA to rBC went down with increase of RH (Figs. 9g and 9h), indicating a
579 trivial role of aqueous/heterogenous oxidation for the SOA coated on rBC observed
580 during this campaign.

581 The aging of OA is generally characterized by the increase of O/C and decrease of
582 H/C (Ng et al., 2011;Zhao et al., 2019).The different aging pathways of OA follow
583 different slopes in the Van Krevelen (VK) diagram (Heald et al., 2010)(Heald et al.,
584 2010). For example, addition of only one oxygen atom to the carbon skeleton results in
585 a slope equal to 0, while replacement of the hydrogen atom with a carboxylic acid group
586 ($-COOH$) results in a slope of -1 without fragmentation (C-C bond breaking), and -0.5
587 with fragmentation (Heald et al., 2010;Ng et al., 2011;Zhao et al., 2019). As presented
588 in Fig. 10a, fitting of all OA data yielded a slope of -0.96 , very close to -1 , suggesting
589 that OA ageing process resembled the hydrogen substitution with a $-COOH$ group

590 (carboxylation). Interestingly, the four OA factors (HOA-rich, WS-HOA, LO-OOA_{rBC}
591 and MO-OOA_{rBC}) aligned almost in a straight line with a slope of -0.77 (Fig. 10a), also
592 close to -1 . Figure S7S8 further reveals that there was a strong anti-correlation between
593 mass fractions of sum of HOA-rich and WS-HOA and sum of LO-OOA_{rBC} and MO-
594 OOA_{rBC} ($r=-0.97$); the slope of fitted line was -0.86 . All these results suggest that OA
595 evolution may contain a channel of photochemical transformations from HOA-rich and
596 WS-HOA to LO-OOA_{rBC} and then to MO-OOA_{rBC}. This result is also in line with the
597 observed decrease of POA_{rBC} and increase of SOA_{rBC} against O_x.

598 CHO⁺, CHO₂⁺ and C₂H₂O₂⁺ are the AMS tracer ions for carbonyl, carboxylic acid
599 and glyoxal, respectively (Wang et al., 2020b; Canagaratna et al., 2015a; Yu et al., 2014).
600 Mass fractions of these three fragment ions presented decreasing trends (or no clear
601 trends) against RH (Fig. S8S9), suggesting again that aqueous processing is not an
602 important pathway in OA evolution during this campaign. Conversely, fractional
603 contributions of these three ions presented increasing trends versus O_x, supporting the
604 dominance of photochemical oxidation pathway (Figs. 10b-d). Figures 10e-g show the
605 scatter plots of H/C versus O/C at different O_x concentrations. The regressed slope was
606 -1.03 for low O_x (<60 ppb) conditions (Fig. 10e), indicating that the OA aging at low
607 O_x level is mainly analogue to the carboxylation process. This result corresponds
608 precisely to the fact that mass fractions of CHO₂⁺ and C₂H₂O₂⁺ increased gradually with
609 O_x at low O_x, whereas that of CHO⁺ remained essentially unchanged (Figs. 10e-g). The
610 fitted slope was -1.14 for moderate O_x conditions (60-80 ppb), and it changed to -0.43
611 for high O_x level (>80 ppb) but correlation became weaker ($r=-0.57$). This result
612 implies that the OA evolution under high O_x conditions might include oxidations by
613 the additions of alcohols, peroxides and carboxylation. In all, the evolution of rBCc OA
614 in Shanghai during this campaign is governed by photochemistry rather than aqueous
615 chemistry, but with different oxidation pathways at different O_x levels.

616

617 3.3.4 Coating time of secondary species onto rBC

618 Although the rBCc organics was dominated by primary sources (Fig. 2g), the
619 diurnal variations of OSc, O/C and H/C of the total organics, were controlled

620 predominantly by the two SOA factors. Correlations between the diurnal cycles of MO-
621 OOA_{rBC}/rBC and OSc were extremely well ($r=0.97$ with OSc and $r=0.98$ with O/C),
622 and those of $LO-OOA_{rBC}$ were also tight ($r=0.91$ with OSc and $r=0.92$ with O/C).
623 The correlations with $LO-OOA_{rBC}$ were a bit weaker than those of $MO-OOA_{rBC}$,
624 indicating that $MO-OOA_{rBC}$ was probably the final products and was more important
625 in governing the overall oxidation level of organic coating. Figure 11a depicts the
626 diurnal variations of SOA_{rBC}/rBC and POA_{rBC}/rBC . Diurnal variations of POA_{rBC}/rBC
627 and rBC were overall similar, while the daily pattern of SOA_{rBC}/rBC was almost
628 opposite to that of rBC . This result likely indicates that most POA_{rBC} species were co-
629 emitted and coated on rBC cores originally, therefore the coating process during rBC
630 lifecycle was mainly relevant with SOA species rather than POA species. This process
631 is mainly through photochemical reactions, including in-situ oxidation of originally
632 coated POA species (for example, oxidation of HOA-rich plus WS-HOA to LO-
633 OOA_{rBC} , then to $MO-OOA_{rBC}$), and partitioning of secondary species formed in gas-
634 phase reactions onto rBC surface. In addition, sulfate and nitrate were both secondarily
635 formed, but sulfate was dominated by photochemical production while nitrate was
636 governed by nocturnal heterogenous formation (as discussed in Section 3.3.2); different
637 diurnal patterns of them (Fig. S6S7) point to different coating processes too.

638 In this regard, we hereby propose a concept of average coating time (ACT), which
639 is used to roughly estimate the timescales required for secondary components coated
640 onto rBC . The specific method is listed as follows:

- 641 1. Move forward the diurnal variation of SA_{rBC}/rBC (SA represents a secondary
642 aerosol species) for n hours to get a new SA_{rBC}/rBC diurnal pattern, labelled as
643 “ $SA_{rBC}/rBC(r-nh\text{-ahead})$ ”. Here, the r value is the linear correlation coefficient between
644 the new SA_{rBC}/rBC diurnal pattern with that of rBC .

- 645 2. Choose the best correlation coefficient ($r-nh\text{-ahead}$), and nh corresponds to the
646 ACT for this secondary component.

647 Diurnal patterns of $LO-OOA_{rBC}/rBC$ and $MO-OOA_{rBC}/rBC$ are depicted in Fig.
648 11b. They were both opposite to the trend of rBC , and they were similar to each other,
649 except that $MO-OOA_{rBC}/rBC$ peaked hours later in the afternoon, signifying that the

650 MO-OOA_{rBC} needs longer time to coated on rBC than LO-OOA_{rBC} does, consistent
651 with the fact that MO-OOA_{rBC} was “more aged”. Correspondingly, we obtained an ACT
652 of 7 hours for MO-OOA_{rBC} (0.35-7h-ahead) and 5 hours for LO-OOA_{rBC} (0.57-5h-
653 ahead) (Fig. 11c) using the method described above. The ACT of sulfate (0.65-7h-ahead)
654 and nitrate (0.30-19h-ahead) were 7 and 19 hours, respectively (Fig. 11d). The results
655 suggest that the rBC emitted mainly in the morning rush hours requires a few hours to
656 be adequately coated by LO-OOA_{rBC}, MO-OOA_{rBC} and sulfate, as these three species
657 are mainly produced in the afternoon by photochemical reactions; while photochemical
658 production of nitrate is insignificant, thus rBC was coated by nitrate until later night
659 when nitrate was formed efficiently by heterogenous N₂O₅ hydrolysis. Note the best *r*
660 values were not high (for example, 0.35 for MO-OOA_{rBC} and 0.30 for nitrate), yet the
661 adjusted trends of all secondary components (Figs. 11c and 11d) matched that of rBC
662 quite well during 3:00~12:00 (*r* of 0.90, 0.91, 0.84 and 0.84 for MO-OOA_{rBC}, LO-
663 OOA_{rBC}, sulfate and nitrate, respectively), likely meaning that daytime variations of
664 two SOAs and sulfate were indeed controlled by the coating process while governing
665 factors of their nighttime variations might be complex, and *vice versa* for nitrate.

666

667 3.4 Size-resolved hygroscopicity of rBCc

668 By using the method in Section 2.3, we calculated the size-resolved hygroscopicity
669 parameters for the total rBCc (κ_{rBCc}) and the coatings materials (κ_{CT}) across the whole
670 campaign. The image plots are illustrated in Figs. 12a and b. Generally, large κ_{rBCc} and
671 κ_{CT} values occurred at big particle sizes, and this result was overall similar to that in
672 Nanjing during winter (Wu et al., 2019). We further illustrate the size-resolved κ_{rBCc} as
673 a function of R_{BC} in Fig. 12c. The figure shows that κ_{rBCc} overall became larger with
674 increasing particle size regardless of the coating thickness. However, there were some
675 (though not significant) relatively high κ_{rBCc} values in the range of 80-150 nm (bottom
676 left and bottom right in Fig. 12c).

677 In Figs. 13a and b, we further determined the average size-resolved κ_{rBCc} and κ_{CT}
678 as a function of coated diameter (D_{rBCc}). Both κ_{rBCc} and κ_{CT} values were relatively high
679 at $D_{rBCc} < 100$ nm and presented slight decreases from 100 to 150 nm. This is distinctive

带格式的: 非突出显示

680 from those observed in Nanjing, where κ_{CT} increased with D_{rBCc} from 50 nm (Wu et al.,
681 2019). From Figs. 5b and 5d, it can be seen the $rBCc$ with $D_{rBCc} < 150$ nm was dominated
682 by a portion of ammonium and sulfate (8-10%) and organics (~60%), of which organics
683 was dominated by WS-HOA. Such composition explains the relatively high
684 hygroscopicity at $D_{rBCc} < 150$ nm as both ammonium sulfate and WS-HOA are
685 hydrophilic; a slight decrease of the hygroscopicity from 100 to 150 nm D_{rBCc} was also
686 a response of decreased mass contributions of ammonium sulfate and WS-HOA (and
687 increase of hydrophobic HOA-rich contribution).

688 Figures 13a and b provide the fitted exponential functions for the mean κ_{rBCc} and
689 κ_{CT} with D_{rBCc} . The equations are: $\kappa_{rBCc}(x) = 0.29 - 0.14 \times \exp(-0.006 \times x)$ and $\kappa_{CT}(x) =$
690 $0.35 - 0.09 \times \exp(-0.003 \times x)$ (x is D_{rBCc} , $150 < x < 1000$ nm). Here, 0.29 and 0.35 are
691 the upper limits of κ_{rBCc} and κ_{CT} , higher than those reported in Nanjing (0.28 and 0.30
692 for κ_{rBCc} and κ_{CT}); yet the increasing rates of κ_{rBCc} and κ_{CT} with D_{rBCc} are 0.14 and 0.09,
693 respectively, which are much lower than those from Nanjing (0.35 and 0.27 for κ_{rBCc}
694 and κ_{CT}) (Wu et al., 2019). Smaller increased contributions of hydrophilic secondary
695 species from 150 to 1000 nm in Shanghai than those from 100 to 1000 nm in Nanjing
696 are likely the cause of smaller increasing rates of hygroscopicity parameters. In addition,
697 it should be noted that the hygroscopicity is not only determined by the bulk
698 composition, but also affected by the phase state of particles. For instance, a recent
699 study reveals that the hygroscopic growth of phase-separated particles (with ammonium
700 sulfate as cores) can be reduced by the secondary organic shells and is dependent on
701 the thickness of organic coating (Li et al., 2021), (Li et al., 2021).

702 The critical supersaturation (SS_C) for a selected dry diameter (D_{rBCc} measured by
703 SP-AMS) of a $rBCc$ particle with a hygroscopicity parameter κ_{rBCc} , can be calculated
704 by the “ κ -Kohler theory” equation (Petters and Kreidenweis, 2007) (Petters and
705 Kreidenweis, 2007). Based on the size-resolved κ_{rBCc} , the CCN activation diameter (D_{50})
706 of particles at a given critical SS_C can be calculated (Wu et al., 2019). Then, by
707 combining the measured $rBCc$ number size distribution and the D_{50} value, activation
708 fraction (f_{AC}) of $rBCc$ number population (i.e., the fraction greater than the D_{50}) can be
709 obtained. Figure 13c shows the SS_C as a function of D_{rBCc} for the entire sampling period

710 to obtain the D_{50} at a specific SS_C . The D_{50} values of the rBC_c particles were determined
711 to be 166 (± 16) nm and 110 (± 5) nm for SS_C of 0.1% and 0.2%, respectively. The two
712 D_{50} values are both smaller than those determined for rBC_c particle in Nanjing (Wu et
713 al., 2019), likely owing to the presence of WS-HOA in Shanghai. Figure 13d shows the
714 f_{AC} at SS_C of 0.1% (D_{50} of 166 nm) was 16 ($\pm 3\%$)%, and the f_{AC} at SS_C of 0.2% (D_{50}
715 of 110 nm) was 59 ($\pm 4\%$)%.

716

717 **3.5 A case study influenced by ship emissions**

718 **3.5.1 Potential source areas of rBC_c**

719 To explore the potential geographic origins of rBC_c at the receptor site, the hybrid
720 single-particle Lagrangian integrated trajectory (HYSPLIT) model (version 4.9) was
721 applied here. Figure 14a shows that the backward trajectories were classified into four
722 air mass clusters, including one long-range transport from northern sea (Cluster1), one
723 long-range transport from northeastern sea (Cluster2), a local one from eastern ports
724 (Cluster3), and one from northwestern inland region (Cluster4). The four clusters
725 occupied 23.8%, 33.8%, 37.3%, and 5.0% of the total trajectories, respectively. It is
726 clear that the sampling period was influenced by offshore air masses in most of the time
727 (95%). Cluster3 had the highest mean rBC_c concentrations ($13.2 \pm 10.9 \mu\text{g m}^{-3}$) while
728 the mean concentrations of the other three clusters were apparently lower (4.3~5.2 μg
729 m^{-3}). This result is plausible as Cluster3 was the shortest in length therefore was least
730 diluted compared with other three clusters. Average chemical compositions of the rBC_c
731 from four clusters (Fig. 14b) showed some differences as well: Cluster1 and Cluster2
732 had higher $MO\text{-}OOA_{rBC}$ contributions, possibly owing to the interceptions of more
733 aged SOA species during the long-range transports; While Cluster4 had less $MO\text{-}$
734 OOA_{rBC} but a bit more POA_{rBC} contributions, likely attributing to more primary species
735 emitted in inland regions (similarly, a higher fraction of nitrate was likely because of
736 enhanced NO_2 emissions).

737

738 **3.5.2 A typical case of rBC_c affected by ship emissions**

739 Ship emissions are found to have an important impact on the air quality of

740 Shanghai and the Yangtze River Delta (Zhao et al., 2013; Fan et al., 2016; Liu et al.,
741 2017b; Chen et al., 2019). The ship engines usually burn heavy fuel oil (HFO), and
742 vanadium (V) and nickel (Ni) can be adopted as reliable tracers for the ship-emitted
743 particles (Ault et al., 2009; Moldanová et al., 2009; Ault et al., 2010). The long-term
744 variation of Ni/V ratio in ship-emitted particles in Shanghai has been recently reported
745 (Yu et al., 2021). The main conclusion is that Ni/V ratio was close to 0.4 in 2018, while
746 it became to be greater than 2.0 in 2020. Our measurement was carried out in 2018, and
747 we therefore chose a period from November 33rd to 55th as a typical case affected by
748 ship emissions (SEP period), since the average Ni/V ratio was ~0.50 and high
749 concentrations of both Ni and V were found. Figure S9S10 shows the concentration-
750 weighted trajectories (CWT) of ship emission tracers (V, Ni), *r*BC and *r*BC-rich factor
751 during SEP, displaying that these components were mainly from sea. During SEP, the
752 correlation coefficient (*r*) between V(Ni) and *r*BC was 0.69 (0.74), indicating the SEP
753 was indeed impacted by ship emissions.

带格式的: 上标

754 Figure 15 displays the chemical characteristics of *r*BC_c and NR-PM₁ components
755 (especially the OA factors), V and Ni, gaseous pollutants and the meteorological
756 parameters during SEP. As a comparison, we also selected a period with no ship
757 emissions with the same time span as SEP (from 0:00 on November 10 to 0:00 on
758 November 12, termed as non-SEP), and a similar plot during non-SEP is presented in
759 Fig. S10S11. During SEP, the wind was mainly from east, and the average wind speed
760 was ~0.5 (± 0.3) m s⁻¹ (Fig. 15a); Wusong, Luojing and Waigaoqiao ports located
761 northeast of the sampling site (Fig. S1). Instead, the wind was mainly from north during
762 non-SEP (Fig. S10aS11a). During SEP, the average mass concentrations of V and Ni
763 were ~~5.8 ng m⁻³~~ $6.3 (\pm 3.1) \text{ ng m}^{-3}$ and ~~3.2-9~~ $(\pm 1.4) \text{ ng m}^{-3}$, respectively, while those
764 during non-SEP were only $2.9 (\pm 1.4) \text{ ng m}^{-3}$ and $2.6 (\pm 1.6) \text{ ng m}^{-3}$. The average mass
765 ratio of V/Ni during SEP was 2.0 in agreement with those reported in ship-influenced
766 PM₁ (Mazzei et al., 2008; Mar et al., 2009), and within the range of 1.9 to 3.5 for
767 domestic HFO (Zhao et al., 2013)(Zhao et al., 2013), while the average ratio of V/Ni
768 (1.1 ± 0.8) during non-SEP was outside the range. Moreover, the major air pollutants
769 emitted from ships include nitrogen oxides (NO_x), sulfur oxides (SO₂), carbon

带格式的: 非上标/下标

770 monoxide (CO), hydrocarbons and primary/secondary particles (Becagli et al.,
771 2017;Wu et al., 2021). As demonstrated in Fig. 15d and Fig. ~~S10d~~S11d, SO₂
772 concentration was overall higher during SEP (10:00-16:00 on November 11 not
773 included); mass loading of NO₂ was higher during the rush hours of non-SEP, but was
774 higher at night (no traffic) during SEP. Mass proportion of sulfate in NR-PM₁ during
775 SEP was also higher than that during non-SEP (~~21.0~~22.7 ± 8.1 % vs. ~~18.7~~19.1 ± 5.3 %),
776 but *vice versa* for nitrate (~~17.8~~17.8 ± 9.9 % during SEP vs. ~~25.4~~26.2 ± 9.1 % during
777 non-SEP).

778 We further investigated the dependences of *r*BCc and NR-PM₁ species on V during
779 SEP and non-SEP, as shown in Fig. ~~S11~~S12. Here we only used V since Ni level might
780 be influenced by other emission sources, such as refining industry (Jang et al.,
781 2007;Kim et al., 2014) in urban Shanghai, and during non-SEP, Ni still presented a good
782 correlation with *r*BC (*r*=0.80). During SEP, V concentrations (most of them >4 ng m⁻³)
783 overall positively correlated with both sulfate and nitrate (except for *r*BCc sulfate) (Fig.
784 ~~S11a~~S12a). Considering that V concentration was independently measured for all fine
785 particles, a better correlation with total NR-PM₁ sulfate than it with *r*BCc sulfate is
786 reasonable. Similarly, V-rich particles had positive correlations with traffic-related OA
787 and LO-OOA no matter in *r*BCc or in total NR-PM₁ (Fig. ~~S11b~~S12b). Conversely,
788 during non-SEP, particles with low-V content (most of them <4 ng m⁻³) had no clear
789 links with sulfate, nitrate, POA and SOA species (even anti-correlations for V>2.5 ng
790 m⁻³) (Figs. ~~S11c~~S12c and ~~S11d~~S12d; a detailed comparison of the correlation
791 coefficients of V with OA factors of *r*BCc and NR-PM₁ organics are provided in Table
792 S2). The results above ~~demonstrate~~demonstrate that during SEP, chemical properties
793 of the particles (both fresh and aged ones) were clearly linked with ship influences.

794 Previous studies (Ault et al., 2009;Ault et al., 2010;Liu et al., 2017b) have shown
795 that the fresh ship-emitted V-rich particles are typically accompanied by high sulfate
796 contribution, while those aged V-containing ship particles are on the other hand with
797 relatively high nitrate contribution. In order to further probe chemical characteristics
798 and evolution processes of particles influenced by ship emissions, we divided SEP into
799 three episodes (i.e., EP1-EP3) (marked in Fig. 15). During EP1, *r*BC content was

800 highest (Fig. 15k) and coating was thinnest (Fig. S12;S13i) indicating the particles were
801 relatively fresh, nevertheless the SOA contents were not low (Figs.15j and 15l), OS_c
802 was moderate (Fig. S12;S13j), sulfate portions in NR-PM₁ and rBC_c were both the
803 highest (26.5%), and nitrate portion was the lowest (9.8%) among three episodes
804 (Figs.15i and 15k). Such composition is not common in other cases, demonstrating it
805 was a specific period impacted by fresh ship emissions. EP2 had the highest mass
806 loadings of V, gas pollutants as well as the lowest planetary boundary layer (PBL)
807 height (~200 meters) (Fig. S12;S13). Mass contributions of nitrate increased and sulfate
808 decreased, and rBC content decreased from those during EP1, signifying that the
809 particle population likely contained some aged ship-emitted particles. ~~Of course~~ Surely,
810 particle composition during EP2 was also influenced by the formation mechanisms of
811 secondary species: EP2 was mostly during nighttime, therefore photochemical
812 formation of sulfate and SOA were weak (~~contributions were low~~ as shown in Figs. 15i-
813 ~~h~~), and 15l, sulfate contribution was only 15.1%, and SOA contribution was only 33.7%),
814 while nitrate formation was enhanced due to the nocturnal process. During EP3, rBC
815 was the lowest, sulfate and V were moderate, nitrate and SOA were highest in both
816 rBC_c and NR-PM₁, OS_c and R_{BC} were highest in rBC_c among the three episodes (Figs.
817 15i-l and Figs. S12;S13i-k), therefore it was also a period with influence from aged
818 ship-emitted particles; the difference from EP2 is that photochemically formed sulfate
819 and SOA were still significant as EP3 was in the later afternoon and early evening,
820 though heterogeneously formed nitrate played a non-negligible role too (see the
821 increase of RH, increase of nitrate and decrease of O₃ concentrations from the
822 beginning of EP3 in Fig. 15).

823

824 **4. Conclusions and implications**

825 We conducted a field measurement during November of 2018 in urban Shanghai,
826 China, focusing on the elucidation of physical and chemical properties of the ambient
827 particles containing rBC cores (rBC_c) by using a laser-only SP-AMS together with a
828 HR-AMS. The campaign-average rBC_c was 4.6 (± 4.4) μg m⁻³, occupying ~19.1 (±
829 4.9)% mass of the total NR-PM₁. The average mass ratio of coating to rBC cores (R_{BC})

830 was ~ 5.0 , (± 1.7), indicating an overall thick coating, compared with the $rBCc$ near
831 combustion source. Sulfate was found to preferentially condense on non- rBC particles
832 thus led to a low fraction of $rBCc$ sulfate to that in NR-PM₁ ($7.4\% \pm 2.2\%$), while
833 distribution of nitrate between $rBCc$ and non- rBC particles showed no obvious
834 difference. PMF analysis on $rBCc$ and NR-PM₁ OA reveals that cooking-related
835 organics were externally mixed with rBC , and a small portion of organics from biomass
836 burning was only present in $rBCc$; the traffic-related OA species, however, was in a
837 large part internally mixed with rBC .

838 A regression algorithm was applied to deconvolute the size distributions of
839 individual $rBCc$ OA factors, and results show that small $rBCc$ particles were
840 predominantly generated from traffic, and such particles could grow bigger because of
841 condensation of secondary inorganic and organic components, resulting in thick coating.
842 Investigation on diurnal patterns of the $rBCc$ species reveals that sulfate and two SOA
843 factors (LO-OOA _{rBC} and MO-OOA _{rBC}) were generated mainly through daytime
844 photochemical oxidation; nitrate, on the other hand, was governed mainly by the
845 nocturnal N₂O₅ hydrolysis. Partial SOA was found to be produced from in-situ
846 photochemical conversion from traffic-related POA. An average coating time (ACT)
847 was proposed to roughly estimate the timescales for the secondary species to coat on
848 rBC , and the ACT of sulfate, LO-OOA _{rBC} , MO-OOA _{rBC} and nitrate were approximately
849 ~~57~~, 5, 7 and 19 hours, respectively.

850 Moreover, the size-resolved hygroscopicity parameters of $rBCc$ particles (κ_{rBCc})
851 and the coating material (κ_{CT}) were obtained based on the elucidated composition of
852 $rBCc$ particles. The fitted equations are: $\kappa_{rBCc}(x) = 0.29 - 0.14 \times \exp(-0.006 \times x)$ and
853 $\kappa_{CT}(x) = 0.35 - 0.09 \times \exp(-0.003 \times x)$ (x is D_{rBCc} , $150 < x < 1000$ nm). The minimums
854 of both κ_{rBCc} and κ_{CT} were at ~ 150 nm due to the abundances of hydrophobic rBC cores
855 and traffic-related HOA at this size. Under critical supersaturations (SS_C) of 0.1% and
856 0.2%, the D_{50} values were estimated to be $166 (\pm 16)$ and $110 (\pm 5)$ nm, and the
857 activated number fractions of $rBCc$ particles were $16 (\pm 3\%)\%$ and $59 (\pm 4\%)\%$,
858 respectively. Finally, a typical case with influence from ship emissions was investigated.
859 During this period, the $rBCc$ particles were enriched in V (on average ~~5.86.3~~ $5.86.3 \pm 3.1$ ng

860 m^{-3}), with a V/Ni ratio of 2.0, (± 0.6), and various secondary formation processes affect
861 the ship-emitted particles at different times of the day.

862 In summary, the findings from this comprehensive study on *rBCc* provide rich
863 information regarding the various primary sources and secondary formation pathways
864 of species coated on *rBC*, as well as the features of distributions of those species
865 between *rBC* and non-*rBC* particles. In particular, different types of *rBCc* particles
866 from diesel and gasoline vehicle emissions were resolved and elucidation of their
867 properties are useful to their future effective control. Understanding of the formation
868 processes and coating timescales of secondary components is helpful to understand the
869 impact of ambient BC particles too. At last, the parameterized relationship of
870 hygroscopicity with size distribution is useful for modelling the climate effect of *rBC*
871 (alternation of cloud properties).

872

873 *Data availability.* The data in this study are available from the authors upon request
874 (caxinra@163.com).

875

876 *Supplement.* The supplement related to this article is available online at: XXX

877

878 *Author contributions.* SJC, DDH, YZW, JFW, FZS, and XLG conducted the field
879 measurement. SJC, DDH, YZW, JFW, and JKX analyzed the data. YJZ, HLW, CH and
880 HL reviewed the paper and provide useful suggestions. SJC and XLG wrote the paper.

881

882 *Competing interests.* The contact author has declared that neither they nor their co-
883 authors have any competing interests.

884

885 *Disclaimer.* Publisher's note: Copernicus Publications remains neutral with regard to
886 jurisdictional claims in published maps and institutional affiliations.

887

888 *Acknowledgements.* We sincerely thank SAES to provide data of gaseous pollutants and
889 particulate V and Ni, and the logistic help during the campaign.

890

891 *Financial support.* This work has been supported by the National Natural Science
892 Foundation of China (42021004 ~~and~~ 21976093 ~~and~~ 21777073).

893

894 *Review statement.* This paper was XXX.

895

896 **References**

897 Aiken, A. C., DeCarlo, P. F., Kroll, J. H., Worsnop, D. R., Huffman, J. A., Docherty,
898 K. S., Ulbrich, I. M., Mohr, C., Kimmel, J. R., Sueper, D., Sun, Y., Zhang, Q., Trimborn,
899 A., Northway, M., Ziemann, P. J., Canagaratna, M. R., Onasch, T. B., Alfarra, M. R.,
900 Prevot, A. S. H., Dommen, J., Duplissy, J., Metzger, A., Baltensperger, U., and Jimenez,
901 J. L.: O/C and OM/OC ratios of primary, secondary, and ambient organic aerosols with
902 high-resolution time-of-flight aerosol mass spectrometry, *Environ. Sci. Technol.*, 42,
903 4478-4485, <https://doi.org/10.1021/es703009q>, 2008.

带格式的: 字体颜色: 超链接

带格式的: 字体颜色: 超链接

904 Ault, A. P., Moore, M. J., Furutani, H., and Prather, K. A.: Impact of emissions
905 from the Los Angeles port region on San Diego air quality during regional transport
906 events, *Environ. Sci. Technol.*, 43, 3500-3506, <https://doi.org/10.1021/es8018918>,
907 2009.

带格式的: 字体颜色: 超链接

带格式的: 字体颜色: 超链接

908 Ault, A. P., Gaston, C. I., Ying, W., Gerardo, D., Thiemens, M. H., and Prather, K.
909 A.: Characterization of the single particle mixing state of individual ship plume events
910 measured at the Port of Los Angeles, *Environ. Sci. Technol.*, 44, 1954-1961,
911 <https://doi.org/10.1021/es902985h>, 2010.

带格式的: 字体颜色: 超链接

带格式的: 字体颜色: 超链接

912 Becagli, S., Anello, F., Bommarito, C., Cassola, F., Calzolari, G., Di Iorio, T., di
913 Sarra, A., Gómez-Amo, J.-L., Lucarelli, F., Marconi, M., Meloni, D., Monteleone, F.,
914 Nava, S., Pace, G., Severi, M., Sferlazzo, D. M., Traversi, R., and Udisti, R.:
915 Constraining the ship contribution to the aerosol of the central Mediterranean, *Atmos.*
916 *Chem. Phys.*, 17, 2067-2084, <https://doi.org/10.5194/acp-17-2067-2017>, 2017.

带格式的: 字体颜色: 超链接

带格式的: 字体颜色: 超链接

917 Bond, T. C., Doherty, S. J., Fahey, D. W., Forster, P. M., Berntsen, T., DeAngelo,
918 B. J., Flanner, M. G., Ghan, S., Kärcher, B., Koch, D., Kinne, S., Kondo, Y., Quinn, P.
919 K., Sarofim, M. C., Schultz, M. G., Schulz, M., Venkataraman, C., Zhang, H., Zhang,

920 S., Bellouin, N., Guttikunda, S. K., Hopke, P. K., Jacobson, M. Z., Kaiser, J. W.,
921 Klimont, Z., Lohmann, U., Schwarz, J. P., Shindell, D., Storelvmo, T., Warren, S. G.,
922 and Zender, C. S.: Bounding the role of black carbon in the climate system: A scientific
923 assessment, *J. Geophys. Res.: Atmos.*, 118, 5380-5552,
924 <https://doi.org/10.1002/jgrd.50171>, 2013.

带格式的: 字体颜色: 超链接

带格式的: 字体颜色: 超链接

925 Canagaratna, M. R., Jayne, J. T., Jimenez, J. L., Allan, J. D., Alfarra, M. R., Zhang,
926 Q., Onasch, T. B., Drewnick, F., Coe, H., Middlebrook, A., Delia, A., Williams, L. R.,
927 Trimborn, A. M., Northway, M. J., DeCarlo, P. F., Kolb, C. E., Davidovits, P., and
928 Worsnop, D. R.: Chemical and microphysical characterization of ambient aerosols with
929 the aerodyne aerosol mass spectrometer, *Mass Spectrom. Rev.*, 26, 185-222,
930 <https://doi.org/10.1002/mas.20115>, 2007.

带格式的: 字体颜色: 超链接

带格式的: 字体颜色: 超链接

931 Canagaratna, M. R., Jimenez, J. L., Kroll, J. H., Chen, Q., Kessler, S. H., Massoli,
932 P., Hildebrandt Ruiz, L., Fortner, E., Williams, L. R., Wilson, K. R., Surratt, J. D.,
933 Donahue, N. M., Jayne, J. T., and Worsnop, D. R.: Elemental ratio measurements of
934 organic compounds using aerosol mass spectrometry: characterization, improved
935 calibration, and implications, *Atmos. Chem. Phys.*, 15, 253-272,
936 <https://doi.org/10.5194/acp-15-253-2015>, 2015a.

带格式的: 字体颜色: 超链接

带格式的: 字体颜色: 超链接

937 Canagaratna, M. R., Massoli, P., Browne, E. C., Franklin, J. P., Wilson, K. R.,
938 Onasch, T. B., Kirchstetter, T. W., Fortner, E. C., Kolb, C. E., Jayne, J. T., Kroll, J. H.,
939 and Worsnop, D. R.: Chemical compositions of black carbon particle cores and coatings
940 via soot particle aerosol mass spectrometry with photoionization and electron ionization,
941 *J. Phys. Chem. A*, 119, 4589-4599, <https://doi.org/10.1021/jp510711u>, 2015b.

带格式的: 字体颜色: 超链接

带格式的: 字体颜色: 超链接

942 Cao, L.-M., Wei, J., He, L.-Y., Zeng, H., Li, M.-L., Zhu, Q., Yu, G.-H., and Huang,
943 X.-F.: Aqueous aging of secondary organic aerosol coating onto black carbon: Insights
944 from simultaneous L-ToF-AMS and SP-AMS measurements at an urban site in
945 southern China, *J. Clean Prod.*, 330, 129888,
946 <https://doi.org/10.1016/j.jclepro.2021.129888>, 2022.

带格式的: 字体颜色: 超链接

带格式的: 字体颜色: 超链接

947 Cappa, C. D., Onasch, T. B., Massoli, P., Worsnop, D. R., Bates, T. S., Cross, E.
948 S., Davidovits, P., Hakala, J., Hayden, K. L., Jobson, B. T., Kolesar, K. R., Lack, D. A.,
949 Lerner, B. M., Li, S.-M., Mellon, D., Nuaaman, I., Olfert, J. S., Petäjä, T., Quinn, P. K.,

950 Song, C., Subramanian, R., Williams, E. J., and Zaveri, R. A.: Radiative Absorption
951 Enhancements Due to the Mixing State of Atmospheric Black Carbon, *Science*, 337,
952 1078-1081, <https://doi.org/10.1126/science.1230260>, 2012.

953 Chang, R. Y. W., Slowik, J. G., Shantz, N. C., Vlasenko, A., Liggio, J., Sjostedt, S.
954 J., Leaitch, W. R., and Abbatt, J. P. D.: The hygroscopicity parameter (κ) of ambient
955 organic aerosol at a field site subject to biogenic and anthropogenic influences:
956 relationship to degree of aerosol oxidation, *Atmos. Chem. Phys.*, 10, 5047-5064,
957 <https://doi.org/10.5194/acp-10-5047-2010>, 2010.

958 Chen, B., Bai, Z., Cui, X., Chen, J., Andersson, A., and Gustafsson, O.: Light
959 absorption enhancement of black carbon from urban haze in Northern China winter,
960 *Environ. Pollut.*, 221, 418-426, <https://doi.org/10.1016/j.envpol.2016.12.004>, 2017.

961 Chen, C., Fan, X., Shaltout, T., Qiu, C., Ma, Y., Goldman, A., and Khalizov, A. F.:
962 An unexpected restructuring of combustion soot aggregates by subnanometer coatings
963 of polycyclic aromatic hydrocarbons, *Geophys. Res. Lett.*, 43, 11,080-011,088,
964 <https://doi.org/10.1002/2016GL070877>, 2016.

965 Chen, C., Enekwizu, O. Y., Fan, X., Dobrzanski, C. D., Ivanova, E. V., Ma, Y., Gor,
966 G. Y., and Khalizov, A. F.: Single Parameter for Predicting the Morphology of
967 Atmospheric Black Carbon, *Environ. Sci. Technol.*, 52, 14169-14179,
968 <https://doi.org/10.1021/acs.est.8b04201>, 2018.

969 Chen, D., Tian, X., Lang, J., Zhou, Y., Li, Y., Guo, X., Wang, W., and Liu, B.: The
970 impact of ship emissions on PM_{2.5} and the deposition of nitrogen and sulfur in Yangtze
971 River Delta, China, *Sci. Total Environ.*, 649, 1609-1619,
972 <https://doi.org/10.1016/j.scitotenv.2018.08.313>, 2019.

973 Clegg, S. L., Brimblecombe, P., and Wexler, A. S.: Thermodynamic model of the
974 system $\text{H}^+ - \text{NH}_4^+ - \text{SO}_4^{2-} - \text{NO}_3^- - \text{H}^+ - \text{NH}_4^+ - \text{SO}_4^{2-} - \text{NO}_3^- - \text{H}_2\text{O}$ at tropospheric
975 temperatures, 102, 2155-2171, <https://doi.org/10.1021/jp973043j>, 1998.

976 Collier, S., Williams, L. R., Onasch, T. B., Cappa, C. D., Zhang, X., Russell, L.
977 M., Chen, C.-L., Sanchez, K. J., Worsnop, D. R., and Zhang, Q.: Influence of Emissions
978 and Aqueous Processing on Particles Containing Black Carbon in a Polluted Urban

带格式的: 字体颜色: 超链接

带格式的: 字体颜色: 超链接

带格式的: 字体颜色: 超链接

带格式的: 字体颜色: 超链接

带格式的: 字体颜色: 超链接

带格式的: 字体颜色: 超链接

带格式的: 字体颜色: 超链接

带格式的: 字体颜色: 超链接

带格式的: 字体颜色: 超链接

带格式的: 字体颜色: 超链接

带格式的: 非上标/下标

带格式的: 字体颜色: 超链接

带格式的: 字体颜色: 超链接

带格式的: 非上标/下标

带格式的: 字体颜色: 超链接

带格式的: 字体颜色: 超链接

979 Environment: Insights From a Soot Particle-Aerosol Mass Spectrometer, *J. Geophys.*
980 *Res.: Atmos.*, 123, 6648-6666, <https://doi.org/10.1002/2017jd027851>, 2018.

981 Corbin, J. C., Sierau, B., Gysel, M., Laborde, M., Keller, A., Kim, J., Petzold, A.,
982 Onasch, T. B., Lohmann, U., and Mensah, A. A.: Mass spectrometry of refractory black
983 carbon particles from six sources: carbon-cluster and oxygenated ions, *Atmos. Chem.*
984 *Phys.*, 14, 2591-2603, <https://doi.org/10.5194/acp-14-2591-2014>, 2014.

985 Cubison, M. J., Ortega, A. M., Hayes, P. L., Farmer, D. K., Day, D., Lechner, M.
986 J., Brune, W. H., Apel, E., Diskin, G. S., Fisher, J. A., Fuelberg, H. E., Hecobian, A.,
987 Knapp, D. J., Mikoviny, T., Riemer, D., Sachse, G. W., Sessions, W., Weber, R. J.,
988 Weinheimer, A. J., Wisthaler, A., and Jimenez, J. L.: Effects of aging on organic aerosol
989 from open biomass burning smoke in aircraft and laboratory studies, *Atmos. Chem.*
990 *Phys.*, 11, 12049-12064, <https://doi.org/10.5194/acp-11-12049-2011>, 2011.

991 DeCarlo, P. F., Kimmel, J. R., Trimborn, A., Northway, M. J., Jayne, J. T., Aiken,
992 A. C., Gonin, M., Fuhrer, K., Horvath, T., Docherty, K. S., Worsnop, D. R., and Jimenez,
993 J. L.: Field-Deployable, High-Resolution, Time-of-Flight Aerosol Mass Spectrometer,
994 *Anal. Chem.*, 78, 8281-8289, <https://doi.org/10.1021/ac061249n>, 2006.

995 Enroth, J., Saarikoski, S., Niemi, J., Kousa, A., Ježek, I., Močnik, G., Carbone, S.,
996 Kuuluvainen, H., Rönkkö, T., Hillamo, R., and Pirjola, L.: Chemical and physical
997 characterization of traffic particles in four different highway environments in the
998 Helsinki metropolitan area, *Atmos. Chem. Phys.*, 16, 5497-5512,
999 <https://doi.org/10.5194/acp-16-5497-2016>, 2016.

1000 Fan, Q., Zhang, Y., Ma, W., Ma, H., Feng, J., Yu, Q., Yang, X., Ng, S. K., Fu, Q.,
1001 and Chen, L.: Spatial and Seasonal Dynamics of Ship Emissions over the Yangtze River
1002 Delta and East China Sea and Their Potential Environmental Influence, *Environ. Sci.*
1003 *Technol.*, 50, 1322-1329, <https://doi.org/10.1021/acs.est.5b03965>, 2016.

1004 Gao, X., Yang, L., Cheng, S., Gao, R., Zhou, Y., Xue, L., Shou, Y., Wang, J., Wang,
1005 X., Nie, W., Xu, P., and Wang, W.: Semi-continuous measurement of water-soluble ions
1006 in PM_{2.5} in Jinan, China: Temporal variations and source apportionments, *Atmos.*
1007 *Environ.*, 45, 6048-6056, <https://doi.org/10.1016/j.atmosenv.2011.07.041>, 2011.

1008 Ge, X., Zhang, Q., Sun, Y., Ruehl, C. R., and Setyan, A.: Effect of aqueous-phase

带格式的: 字体颜色: 超链接

带格式的: 字体颜色: 超链接

带格式的: 字体颜色: 超链接

带格式的: 字体颜色: 超链接

带格式的: 字体颜色: 超链接

带格式的: 字体颜色: 超链接

带格式的: 字体颜色: 超链接

带格式的: 字体颜色: 超链接

带格式的: 字体颜色: 超链接

带格式的: 字体颜色: 超链接

带格式的: 字体颜色: 超链接

带格式的: 字体颜色: 超链接

带格式的: 非上标/下标

带格式的: 字体颜色: 超链接

带格式的: 字体颜色: 超链接

1009 processing on aerosol chemistry and size distributions in Fresno, California, during
1010 wintertime, Environ. Chem., 9, 221-235, <https://doi.org/10.1071/EN11168>, 2012.

带格式的: 字体颜色: 超链接

带格式的: 字体颜色: 超链接

1011 Gilardoni, S., Massoli, P., Paglione, M., Giulianelli, L., Carbone, C., Rinaldi, M.,
1012 Decesari, S., Sandrini, S., Costabile, F., Gobbi, G. P., Pietrogrande, M. C., Visentin, M.,
1013 Scotto, F., Fuzzi, S., and Facchini, M. C.: Direct observation of aqueous secondary
1014 organic aerosol from biomass-burning emissions, Proc. Natl. Acad. Sci. U. S. A., 113,
1015 10013-10018, <https://doi.org/10.1073/pnas.1602212113>, 2016.

带格式的: 字体颜色: 超链接

带格式的: 字体颜色: 超链接

1016 Gong, X., Zhang, C., Chen, H., Nizkorodov, S. A., Chen, J., and Yang, X.: Size
1017 distribution and mixing state of black carbon particles during a heavy air pollution
1018 episode in Shanghai, Atmos. Chem. Phys., 16, 5399-5411, [https://doi.org/10.5194/acp-](https://doi.org/10.5194/acp-16-5399-2016)
1019 [16-5399-2016](https://doi.org/10.5194/acp-16-5399-2016), 2016.

带格式的: 字体颜色: 超链接

带格式的: 字体颜色: 超链接

1020 Gysel, M., Crosier, J., Topping, D. O., Whitehead, J. D., Bower, K. N., Cubison,
1021 M. J., Williams, P. I., Flynn, M. J., McFiggans, G. B., and Coe, H.: Closure study
1022 between chemical composition and hygroscopic growth of aerosol particles during
1023 TORCH2, Atmos. Chem. Phys., 7, 6131-6144, [https://doi.org/10.5194/acp-7-6131-](https://doi.org/10.5194/acp-7-6131-2007)
1024 [2007](https://doi.org/10.5194/acp-7-6131-2007), 2007.

带格式的: 字体颜色: 超链接

带格式的: 字体颜色: 超链接

1025 Heald, C. L., Kroll, J. H., Jimenez, J. L., Docherty, K. S., DeCarlo, P. F., Aiken, A.
1026 C., Chen, Q., Martin, S. T., Farmer, D. K., and Artaxo, P.: A simplified description of
1027 the evolution of organic aerosol composition in the atmosphere, Geophys. Res. Lett.,
1028 37, <https://doi.org/10.1029/2010gl042737>, 2010.

带格式的: 字体颜色: 超链接

带格式的: 字体颜色: 超链接

1029 Hu, D., Liu, D., Kong, S., Zhao, D., Wu, Y., Li, S., Ding, S., Zheng, S., Cheng, Y.,
1030 Hu, K., Deng, Z., Wu, Y., Tian, P., Liu, Q., Huang, M., and Ding, D.: Direct
1031 Quantification of Droplet Activation of Ambient Black Carbon Under Water
1032 Supersaturation, J. Geophys. Res.: Atmos., 126, e2021JD034649,
1033 <https://doi.org/10.1029/2021jd034649>, 2021.

带格式的: 字体颜色: 超链接

带格式的: 字体颜色: 超链接

1034 Jacobi, H. W., Lim, S., Ménégou, M., Ginot, P., Laj, P., Bonasoni, P., Stocchi, P.,
1035 Marinoni, A., and Arnaud, Y.: Black carbon in snow in the upper Himalayan Khumbu
1036 Valley, Nepal: observations and modeling of the impact on snow albedo, melting, and
1037 radiative forcing, The Cryosphere, 9, 1685-1699, [https://doi.org/10.5194/tc-9-1685-](https://doi.org/10.5194/tc-9-1685-2015)
1038 [2015](https://doi.org/10.5194/tc-9-1685-2015), 2015.

带格式的: 字体颜色: 超链接

带格式的: 字体颜色: 超链接

1039 Jang, H.-N., Seo, Y.-C., Lee, J.-H., Hwang, K.-W., Yoo, J.-I., Sok, C.-H., and Kim,
1040 S.-H.: Formation of fine particles enriched by V and Ni from heavy oil combustion:
1041 ~~anthropogenic~~**Anthropogenic** sources and drop-tube furnace experiments, Atmos.
1042 Environ., 41, 1053-1063, <https://doi.org/10.1016/j.atmosenv.2006.09.011>, 2007.

带格式的: 字体颜色: 超链接

带格式的: 字体颜色: 超链接

1043 Jayne, J. T., Leard, D. C., Zhang, X., Davidovits, P., Smith, K. A., Kolb, C. E., and
1044 Worsnop, D. R.: Development of an aerosol mass spectrometer for size and composition
1045 analysis of submicron particles, Aerosol Sci. Technol., 33, 49-70,
1046 <https://doi.org/10.1080/027868200410840>, 2000.

带格式的: 字体颜色: 超链接

带格式的: 字体颜色: 超链接

1047 Kim, K.-H., Shon, Z.-H., Maulida, P. T., and Song, S.-K.: Long-term monitoring
1048 of airborne nickel (Ni) pollution in association with some potential source processes in
1049 the urban environment, Chemosphere, 111, 312-319,
1050 <https://doi.org/10.1016/j.chemosphere.2014.03.138>, 2014.

带格式的: 字体颜色: 超链接

带格式的: 字体颜色: 超链接

1051 Kroll, J. H., Donahue, N. M., Jimenez, J. L., Kessler, S. H., Canagaratna, M. R.,
1052 Wilson, K. R., Altieri, K. E., Mazzoleni, L. R., Wozniak, A. S., Bluhm, H., Mysak, E.
1053 R., Smith, J. D., Kolb, C. E., and Worsnop, D. R.: Carbon oxidation state as a metric
1054 for describing the chemistry of atmospheric organic aerosol, Nat. Chem., 3, 133-139,
1055 <https://doi.org/10.1038/nchem.948>, 2011.

带格式的: 字体颜色: 超链接

带格式的: 字体颜色: 超链接

1056 Lambe, A. T., Ahern, A. T., Wright, J. P., Croasdale, D. R., Davidovits, P., and
1057 Onasch, T. B.: Oxidative aging and cloud condensation nuclei activation of laboratory
1058 combustion soot, J. Aerosol. Sci., 79, 31-39,
1059 <https://doi.org/10.1016/j.jaerosci.2014.10.001>, 2015.

带格式的: 字体颜色: 超链接

带格式的: 字体颜色: 超链接

1060 Laskin, A., Smith, J. S., and Laskin, J.: Molecular characterization of nitrogen-
1061 containing organic compounds in biomass burning aerosols using high-resolution mass
1062 spectrometry, Environ. Sci. Technol., 43, 3764-3771,
1063 <https://doi.org/10.1021/es803456n>, 2009.

带格式的: 字体颜色: 超链接

带格式的: 字体颜色: 超链接

1064 Lee, A. K. Y., Willis, M. D., Healy, R. M., Onasch, T. B., and Abbatt, J. P. D.:
1065 Mixing state of carbonaceous aerosol in an urban environment: single particle
1066 characterization using the soot particle aerosol mass spectrometer (SP-AMS), Atmos.
1067 Chem. Phys., 15, 1823-1841, <https://doi.org/10.5194/acp-15-1823-2015>, 2015.

带格式的: 字体颜色: 超链接

带格式的: 字体颜色: 超链接

1068 Lee, A. K. Y., Chen, C.-L., Liu, J., Price, D. J., Betha, R., Russell, L. M., Zhang,

1069 X., and Cappa, C. D.: Formation of secondary organic aerosol coating on black carbon
1070 particles near vehicular emissions, *Atmos. Chem. Phys.*, 17, 15055-15067,
1071 <https://doi.org/10.5194/acp-17-15055-2017>, 2017.

带格式的: 字体颜色: 超链接

带格式的: 字体颜色: 超链接

1072 Lee, A. K. Y., Rivellini, L. H., Chen, C. L., Liu, J., Price, D. J., Betha, R., Russell,
1073 L. M., Zhang, X., and Cappa, C. D.: Influences of primary emission and secondary
1074 coating formation on the particle diversity and mixing state of black carbon particles,
1075 *Environ. Sci. Technol.*, 53, 9429-9438, <https://doi.org/10.1021/acs.est.9b03064>, 2019.

带格式的: 字体颜色: 超链接

带格式的: 字体颜色: 超链接

1076 Li, W., Teng, X., Chen, X., Liu, L., Xu, L., Zhang, J., Wang, Y., Zhang, Y., and Shi,
1077 Z.: Organic coating reduces hygroscopic growth of phase-separated aerosol particles,
1078 *Environ. Sci. Technol.*, 55, 16339-16346, <https://doi.org/10.1021/acs.est.1c05901>,
1079 2021.

带格式的: 字体颜色: 超链接

带格式的: 字体颜色: 超链接

1080 Liu, D., Allan, J., Whitehead, J., Young, D., Flynn, M., Coe, H., McFiggans, G.,
1081 Fleming, Z. L., and Bandy, B.: Ambient black carbon particle hygroscopic properties
1082 controlled by mixing state and composition, *Atmos. Chem. Phys.*, 13, 2015-2029,
1083 <https://doi.org/10.5194/acp-13-2015-2013>, 2013.

带格式的: 字体颜色: 超链接

带格式的: 字体颜色: 超链接

1084 Liu, D., Whitehead, J., Alfarra, M. R., Reyes-Villegas, E., Spracklen, Dominick V.,
1085 Reddington, Carly L., Kong, S., Williams, Paul I., Ting, Y.-C., Haslett, S., Taylor,
1086 Jonathan W., Flynn, Michael J., Morgan, William T., McFiggans, G., Coe, H., and
1087 Allan, James D.: Black-carbon absorption enhancement in the atmosphere determined
1088 by particle mixing state, *Nat. Geosci.*, 10, 184-188, <https://doi.org/10.1038/ngeo2901>,
1089 2017a.

带格式的: 字体颜色: 超链接

带格式的: 字体颜色: 超链接

1090 Liu, D., Joshi, R., Wang, J., Yu, C., Allan, J. D., Coe, H., Flynn, M. J., Xie, C., Lee,
1091 J., Squires, F., Kotthaus, S., Grimmond, S., Ge, X., Sun, Y., and Fu, P.: Contrasting
1092 physical properties of black carbon in urban Beijing between winter and summer,
1093 *Atmos. Chem. Phys.*, 19, 6749-6769, <https://doi.org/10.5194/acp-19-6749-2019>, 2019.

带格式的: 字体颜色: 超链接

带格式的: 字体颜色: 超链接

1094 Liu, S., Aiken, A. C., Gorkowski, K., Dubey, M. K., Cappa, C. D., Williams, L. R.,
1095 Herndon, S. C., Massoli, P., Fortner, E. C., Chhabra, P. S., Brooks, W. A., Onasch, T.
1096 B., Jayne, J. T., Worsnop, D. R., China, S., Sharma, N., Mazzoleni, C., Xu, L., Ng, N.
1097 L., Liu, D., Allan, J. D., Lee, J. D., Fleming, Z. L., Mohr, C., Zotter, P., Szidat, S., and
1098 Prevot, A. S. H.: Enhanced light absorption by mixed source black and brown carbon

1099 particles in UK winter, Nat. Commun., 6, 8435, <https://doi.org/10.1038/ncomms9435>,
1100 2015.

带格式的: 字体颜色: 超链接

带格式的: 字体颜色: 超链接

1101 Liu, Z., Lu, X., Feng, J., Fan, Q., Zhang, Y., and Yang, X.: Influence of ~~ship~~
1102 ~~emissions~~[Ship Emissions](#) on ~~urban air quality: a~~[Urban Air Quality: A Comprehensive](#)
1103 ~~study using highly time resolved online measurements~~[Study Using Highly Time-](#)
1104 ~~Resolved Online Measurements~~ and ~~numerical simulation~~[Numerical Simulation](#) in
1105 Shanghai, Environ. Sci. Technol., 51, 202-211, <https://doi.org/10.1021/acs.est.6b03834>,
1106 2017b.

带格式的: 字体颜色: 超链接

带格式的: 字体颜色: 超链接

1107 [Ma, Y., Huang, C., Jabbour, H., Zheng, Z., Wang, Y., Jiang, Y., Zhu, W., Ge, X.,](#)
1108 [Collier, S., and Zheng, J.: Mixing state and light absorption enhancement of black](#)
1109 [carbon aerosols in summertime Nanjing, China, Atmos. Environ., 222, 117141,](#)
1110 <https://doi.org/https://doi.org/10.1016/j.atmosenv.2019.117141>, 2020.

1111 Malmborg, V. B., Eriksson, A. C., Shen, M., Nilsson, P., Gallo, Y., Waldheim, B.,
1112 Martinsson, J., Andersson, O., and Pagels, J.: Evolution of In-Cylinder Diesel Engine
1113 Soot and Emission Characteristics Investigated with Online Aerosol Mass Spectrometry,
1114 Environ. Sci. Technol., 51, 1876-1885, <https://doi.org/10.1021/acs.est.6b03391>, 2017.

带格式的: 字体颜色: 超链接

带格式的: 字体颜色: 超链接

1115 Mar, V., Fulvio, A., Andrés, A., Xavier, Q., Teresa, M., Saúl García, D. S., María
1116 Dolores, H., and Rosalía, F. P.: Chemical tracers of particulate emissions from
1117 commercial shipping, Environ. Sci. Technol., 43, 7472-7477,
1118 <https://doi.org/10.1021/es901558t>, 2009.

带格式的: 字体颜色: 超链接

带格式的: 字体颜色: 超链接

1119 Massoli, P., Fortner, E. C., Canagaratna, M. R., Williams, L. R., Zhang, Q., Sun,
1120 Y., Schwab, J. J., Trimborn, A., Onasch, T. B., Demerjian, K. L., Kolb, C. E., Worsnop,
1121 D. R., and Jayne, J. T.: Pollution Gradients and Chemical Characterization
1122 of Particulate Matter from Vehicular Traffic near Major Roadways: Results from the
1123 2009 Queens College Air Quality Study in NYC, Aerosol Sci. Technol., 46, 1201-1218,
1124 <https://doi.org/10.1080/02786826.2012.701784>, 2012.

带格式的: 字体颜色: 超链接

带格式的: 字体颜色: 超链接

1125 Massoli, P., Onasch, T. B., Cappa, C. D., Nuamaan, I., Hakala, J., Hayden, K., Li,
1126 S.-M., Sueper, D. T., Bates, T. S., Quinn, P. K., Jayne, J. T., and Worsnop, D. R.:
1127 Characterization of black carbon-containing particles from soot particle aerosol mass
1128 spectrometer measurements on the R/VAtlantis during CalNex 2010, J. Geophys. Res.:

1129 Atmos., 120, 2575-2593, <https://doi.org/10.1002/2014jd022834>, 2015.

1130 Mazzei, F., D'Alessandro, A., Lucarelli, F., Nava, S., Prati, P., Valli, G., and Vecchi,

1131 R.: Characterization of particulate matter sources in an urban environment, *Sci. Total*

1132 *Environ.*, 401, 81-89, <https://doi.org/10.1016/j.scitotenv.2008.03.008>, 2008.

1133 Mohr, C., Huffman, J. A., Cubison, M. J., Aiken, A. C., Docherty, K. S., Kimmel,

1134 J. R., Ulbrich, I. M., Hannigan, M., and Jimenez, J. L.: Characterization of Primary

1135 Organic Aerosol Emissions from Meat Cooking, Trash Burning, and Motor Vehicles

1136 with High-Resolution Aerosol Mass Spectrometry and Comparison with Ambient and

1137 Chamber Observations, *Environ. Sci. Technol.*, 43, 2443-2449,

1138 <https://doi.org/10.1021/es8011518>, 2009.

1139 Moldanová, J., Fridell, E., Popovicheva, O., Demirdjian, B., Tishkova, V.,

1140 Faccineto, A., and Focsa, C.: Characterisation of particulate matter and gaseous

1141 emissions from a large ship diesel engine, *Atmos. Environ.*, 43, 2632-2641,

1142 <https://doi.org/10.1016/j.atmosenv.2009.02.008>, 2009.

1143 Ng, N. L., Canagaratna, M. R., Jimenez, J. L., Chhabra, P. S., Seinfeld, J. H., and

1144 Worsnop, D. R.: Changes in organic aerosol composition with aging inferred from

1145 aerosol mass spectra, *Atmos. Chem. Phys.*, 11, 6465-6474, [https://doi.org/10.5194/acp-](https://doi.org/10.5194/acp-11-6465-2011)

1146 [11-6465-2011](https://doi.org/10.5194/acp-11-6465-2011), 2011.

1147 Onasch, T. B., Trimborn, A., Fortner, E. C., Jayne, J. T., Kok, G. L., Williams, L.

1148 R., Davidovits, P., and Worsnop, D. R.: Soot Particle Aerosol Mass Spectrometer:

1149 Development, Validation, and Initial Application, *Aerosol Sci. Technol.*, 46, 804-817,

1150 <https://doi.org/10.1080/02786826.2012.663948>, 2012.

1151 Paatero, P., and Tapper, U.: Positive matrix factorization: A non-negative factor

1152 model with optimal utilization of error estimates of data values, *Environmetrics*, 5, 111-

1153 126, <https://doi.org/10.1002/env.3170050203>, 1994.

1154 Pathak, R. K., Wang, T., and Wu, W. S.: Nighttime enhancement of PM_{2.5} nitrate

1155 in ammonia-poor atmospheric conditions in Beijing and Shanghai: Plausible

1156 contributions of heterogeneous hydrolysis of N₂O₅ and HNO₃ partitioning, *Atmos.*

1157 *Environ.*, 45, 1183-1191, <https://doi.org/10.1016/j.atmosenv.2010.09.003>, 2011.

1158 Peng, J., Hu, M., Guo, S., Du, Z., Zheng, J., Shang, D., Levy, Z. M., Zeng, L.,

带格式的: 字体颜色: 超链接

带格式的: 字体颜色: 超链接

带格式的: 字体颜色: 超链接

带格式的: 字体颜色: 超链接

带格式的: 字体颜色: 超链接

带格式的: 字体颜色: 超链接

带格式的: 字体颜色: 超链接

带格式的: 字体颜色: 超链接

带格式的: 字体颜色: 超链接

带格式的: 字体颜色: 超链接

带格式的: 字体颜色: 超链接

带格式的: 字体颜色: 超链接

带格式的: 字体颜色: 超链接

带格式的: 字体颜色: 超链接

带格式的: 非上标/ 下标

带格式的: 非上标/ 下标

带格式的: 非上标/ 下标

带格式的: 非上标/ 下标

带格式的: 字体颜色: 超链接

带格式的: 字体颜色: 超链接

1159 Shao, M., and Wu, Y. S.: Markedly enhanced absorption and direct radiative forcing of
1160 black carbon under polluted urban environments, Proc. Natl. Acad. Sci. U. S. A., 113,
1161 4266-4271, <https://doi.org/10.1073/pnas.1602310113>, 2016.

带格式的: 字体颜色: 超链接

带格式的: 字体颜色: 超链接

1162 Petit, J. E., Favez, O., Albinet, A., and Canonaco, F.: A user-friendly tool for
1163 comprehensive evaluation of the geographical origins of atmospheric pollution: Wind
1164 and trajectory analyses, 88, 183-187, <https://doi.org/10.1016/j.envsoft.2016.11.022>,
1165 2017.

带格式的: 字体颜色: 超链接

带格式的: 字体颜色: 超链接

1166 Petters, M. D., and Kreidenweis, S. M.: A single parameter representation of
1167 hygroscopic growth and cloud condensation nucleus activity, Atmos. Chem. Phys., 7,
1168 1961-1971, <https://doi.org/10.5194/acp-7-1961-2007>, 2007.

带格式的: 字体颜色: 超链接

带格式的: 字体颜色: 超链接

1169 Ramanathan, V., and Carmichael, G.: Global and regional climate changes due to
1170 black carbon, Nat. Geosci., 1, 221-227, <https://doi.org/10.1038/ngeo156>, 2008.

带格式的: 字体颜色: 超链接

带格式的: 字体颜色: 超链接

1171 Rivellini, L.-H., Adam, M. G., Kasthuriarachchi, N., and Lee, A. K. Y.:
1172 Characterization of carbonaceous aerosols in Singapore: insight from black carbon
1173 fragments and trace metal ions detected by a soot particle aerosol mass spectrometer,
1174 Atmos. Chem. Phys., 20, 5977-5993, <https://doi.org/10.5194/acp-20-5977-2020>, 2020.

带格式的: 字体颜色: 超链接

带格式的: 字体颜色: 超链接

1175 Saarikoski, S., Timonen, H., Carbone, S., Kuuluvainen, H., Niemi, J. V., Kousa,
1176 A., Rönkkö, T., Worsnop, D., Hillamo, R., and Pirjola, L.: Investigating the chemical
1177 species in submicron particles emitted by city buses, Aerosol Sci. Technol., 51, 317-
1178 329, <https://doi.org/10.1080/02786826.2016.1261992>, 2016.

带格式的: 字体颜色: 超链接

带格式的: 字体颜色: 超链接

1179 Sun, Y. L., Zhang, Q., Schwab, J. J., Demerjian, K. L., Chen, W. N., Bae, M. S.,
1180 Hung, H. M., Hogrefe, O., Frank, B., Rattigan, O. V., and Lin, Y. C.: Characterization
1181 of the sources and processes of organic and inorganic aerosols in New York city with a
1182 high-resolution time-of-flight aerosol mass spectrometer, Atmos. Chem. Phys., 11,
1183 1581-1602, <https://doi.org/10.5194/acp-11-1581-2011>, 2011.

带格式的: 字体颜色: 超链接

带格式的: 字体颜色: 超链接

1184 Sun, Y. L., Zhang, Q., Schwab, J. J., Yang, T., Ng, N. L., and Demerjian, K. L.:
1185 Factor analysis of combined organic and inorganic aerosol mass spectra from high
1186 resolution aerosol mass spectrometer measurements, Atmos. Chem. Phys., 12, 8537-
1187 8551, <https://doi.org/10.5194/acp-12-8537-2012>, 2012.

带格式的: 字体颜色: 超链接

带格式的: 字体颜色: 超链接

1188 Topping, D. O., McFiggans, G. B., and Coe, H.: A curved multi-component aerosol

1189 hygroscopicity model framework: Part 1—~~Inorganic~~2—Including organic compounds,
1190 Atmos. Chem. Phys., 5, ~~1205-1222~~1223-1242, [带格式的: 字体颜色: 超链接](https://doi.org/10.5194/acp-5-
1191 1205<u>1223-2005</u>, 2005a.</p></div><div data-bbox=)

域代码已更改

带格式的: 字体颜色: 超链接

带格式的: 字体颜色: 超链接

1192 Topping, D. O., McFiggans, G. B., and Coe, H.: A curved multi-component aerosol
1193 hygroscopicity model framework: Part 2—~~Including organic~~1—Inorganic compounds,
1194 Atmos. Chem. Phys., 5, ~~1223-1242~~1205-1222, [1196 Ulbrich, I. M., Canagaratna, M. R., Zhang, Q., Worsnop, D. R., and Jimenez, J. L.:
1197 Interpretation of organic components from Positive Matrix Factorization of aerosol
1198 mass spectrometric data, Atmos. Chem. Phys., 9, 2891-2918,
1199 <https://doi.org/10.5194/acp-9-2891-2009>, 2009.](https://doi.org/10.5194/acp-5-
1195 1223<u>1205-2005</u>, 2005b.</p></div><div data-bbox=)

带格式的: 字体颜色: 超链接

带格式的: 字体颜色: 超链接

1200 Ulbrich, I. M., Canagaratna, M. R., Cubison, M. J., Zhang, Q., Ng, N. L., Aiken,
1201 A. C., and Jimenez, J. L.: Three-dimensional factorization of size-resolved organic
1202 aerosol mass spectra from Mexico City, Atmos. Meas. Tech., 5, 195-224,
1203 <https://doi.org/10.5194/amt-5-195-2012>, 2012.

带格式的: 字体颜色: 超链接

带格式的: 字体颜色: 超链接

1204 Wang, J., Ge, X., Chen, Y., Shen, Y., Zhang, Q., Sun, Y., Xu, J., Ge, S., Yu, H., and
1205 Chen, M.: Highly time-resolved urban aerosol characteristics during springtime in
1206 Yangtze River Delta, China: insights from soot particle aerosol mass spectrometry,
1207 Atmos. Chem. Phys., 16, 9109-9127, <https://doi.org/10.5194/acp-16-9109-2016>, 2016.

带格式的: 字体颜色: 超链接

带格式的: 字体颜色: 超链接

1208 Wang, J., Zhang, Q., Chen, M., Collier, S., Zhou, S., Ge, X., Xu, J., Shi, J., Xie,
1209 C., Hu, J., Ge, S., Sun, Y., and Coe, H.: First Chemical Characterization of Refractory
1210 Black Carbon Aerosols and Associated Coatings over the Tibetan Plateau (4730 m a.s.l),
1211 Environ. Sci. Technol., 51, 14072-14082, <https://doi.org/10.1021/acs.est.7b03973>,
1212 2017.

带格式的: 字体颜色: 超链接

带格式的: 字体颜色: 超链接

1213 Wang, J., Liu, D., Ge, X., Wu, Y., Shen, F., Chen, M., Zhao, J., Xie, C., Wang, Q.,
1214 Xu, W., Zhang, J., Hu, J., Allan, J., Joshi, R., Fu, P., Coe, H., and Sun, Y.:
1215 Characterization of black carbon-containing fine particles in Beijing during wintertime,
1216 Atmos. Chem. Phys., 19, 447-458, <https://doi.org/10.5194/acp-19-447-2019>, 2019.

带格式的: 字体颜色: 超链接

带格式的: 字体颜色: 超链接

1217 Wang, J., Ye, J., Liu, D., Wu, Y., Zhao, J., Xu, W., Xie, C., Shen, F., Zhang, J.,
1218 Ohno, P. E., Qin, Y., Zhao, X., Martin, S. T., Lee, A. K. Y., Fu, P., Jacob, D. J., Zhang,

1219 Q., Sun, Y., Chen, M., and Ge, X.: Characterization of submicron organic particles in
1220 Beijing during summertime: comparison between SP-AMS and HR-AMS, *Atmos.*
1221 *Chem. Phys.*, 20, 14091-14102, <https://doi.org/10.5194/acp-20-14091-2020>, 2020a.

1222 Wang, J., Ye, J., Zhang, Q., Zhao, J., Wu, Y., Li, J., Liu, D., Li, W., Zhang, Y., Wu,
1223 C., Xie, C., Qin, Y., Lei, Y., Huang, X., Guo, J., Liu, P., Fu, P., Li, Y., Lee, H. C., Choi,
1224 H., Zhang, J., Liao, H., Chen, M., Sun, Y., Ge, X., Martin, S. T., and Jacob, D. J.:
1225 Aqueous production of secondary organic aerosol from fossil-fuel emissions in winter
1226 Beijing haze, *Proc. Natl. Acad. Sci. U. S. A.*, 118, e2022179118,
1227 <https://doi.org/10.1073/pnas.2022179118>, 2021.

1228 Wang, S., Newland, M. J., Deng, W., Rickard, A. R., Hamilton, J. F., Muñoz, A.,
1229 Ródenas, M., Vázquez, M. M., Wang, L., and Wang, X.: Aromatic Photo-oxidation, A
1230 New Source of Atmospheric Acidity, *Environ. Sci. Technol.*, 54, 7798-7806,
1231 <https://doi.org/10.1021/acs.est.0c00526>, 2020b.

1232 Willis, M. D., Healy, R. M., Riemer, N., West, M., Wang, J. M., Jeong, C.-H.,
1233 Wenger, J. C., Evans, G. J., Abbatt, J. P. D., and Lee, A. K. Y.: Quantification of black
1234 carbon mixing state from traffic: implications for aerosol optical properties, *Atmos.*
1235 *Chem. Phys.*, 16, 4693-4706, <https://doi.org/10.5194/acp-16-4693-2016>, 2016.

1236 Wu, Y., Ge, X., Wang, J., Shen, Y., Ye, Z., Ge, S., Wu, Y., Yu, H., and Chen, M.:
1237 Responses of secondary aerosols to relative humidity and photochemical activities in
1238 an industrialized environment during late winter, *Atmos. Environ.*, 193, 66-78,
1239 <https://doi.org/10.1016/j.atmosenv.2018.09.008>, 2018.

1240 Wu, Y., Liu, D., Wang, J., Shen, F., Chen, Y., Cui, S., Ge, S., Wu, Y., Chen, M.,
1241 and Ge, X.: Characterization of Size-Resolved Hygroscopicity of Black Carbon-
1242 Containing Particle in Urban Environment, *Environ. Sci. Technol.*, 53, 14212-14221,
1243 <https://doi.org/10.1021/acs.est.9b05546>, 2019.

1244 Wu, Y., Liu, D., Wang, X., Li, S., Zhang, J., Qiu, H., Ding, S., Hu, K., Li, W., Tian,
1245 P., Liu, Q., Zhao, D., Ma, E., Chen, M., Xu, H., Ouyang, B., Chen, Y., Kong, S., Ge, X.,
1246 and Liu, H.: Ambient marine shipping emissions determined by vessel operation mode
1247 along the East China Sea, *Sci. Total Environ.*, 769, 144713,
1248 <https://doi.org/10.1016/j.scitotenv.2020.144713>, 2021.

带格式的: 字体颜色: 超链接

带格式的: 字体颜色: 超链接

带格式的: 字体颜色: 超链接

带格式的: 字体颜色: 超链接

带格式的: 字体颜色: 超链接

带格式的: 字体颜色: 超链接

带格式的: 字体颜色: 超链接

带格式的: 字体颜色: 超链接

带格式的: 字体颜色: 超链接

带格式的: 字体颜色: 超链接

带格式的: 字体颜色: 超链接

带格式的: 字体颜色: 超链接

带格式的: 字体颜色: 超链接

带格式的: 字体颜色: 超链接

1249 Wu, Z. J., Zheng, J., Shang, D. J., Du, Z. F., Wu, Y. S., Zeng, L. M., Wiedensohler,
1250 A., and Hu, M.: Particle hygroscopicity and its link to chemical composition in the
1251 urban atmosphere of Beijing, China, during summertime, *Atmos. Chem. Phys.*, 16,
1252 1123-1138, <https://doi.org/10.5194/acp-16-1123-2016>, 2016.

带格式的: 字体颜色: 超链接

带格式的: 字体颜色: 超链接

1253 Xie, C., Xu, W., Wang, J., Liu, D., Ge, X., Zhang, Q., Wang, Q., Du, W., Zhao, J.,
1254 Zhou, W., Li, J., Fu, P., Wang, Z., Worsnop, D., and Sun, Y.: Light absorption
1255 enhancement of black carbon in urban Beijing in summer, *Atmos. Environ.*, 213, 499-
1256 504, <https://doi.org/10.1016/j.atmosenv.2019.06.041>, 2019.

带格式的: 字体颜色: 超链接

带格式的: 字体颜色: 超链接

1257 Xu, J., Zhang, Q., Chen, M., Ge, X., Ren, J., and Qin, D.: Chemical composition,
1258 sources, and processes of urban aerosols during summertime in northwest China:
1259 insights from high-resolution aerosol mass spectrometry, *Atmos. Chem. Phys.*, 14,
1260 12593-12611, <https://doi.org/10.5194/acp-14-12593-2014>, 2014.

带格式的: 字体颜色: 超链接

带格式的: 字体颜色: 超链接

1261 Xu, W., Han, T., Du, W., Wang, Q., Chen, C., Zhao, J., Zhang, Y., Li, J., Fu, P.,
1262 Wang, Z., Worsnop, D. R., and Sun, Y.: Effects of Aqueous-Phase and Photochemical
1263 Processing on Secondary Organic Aerosol Formation and Evolution in Beijing, China,
1264 *Environ. Sci. Technol.*, 51, 762-770, <https://doi.org/10.1021/acs.est.6b04498>, 2017.

带格式的: 字体颜色: 超链接

带格式的: 字体颜色: 超链接

1265 Xu, W., Sun, Y., Wang, Q., Zhao, J., Wang, J., Ge, X., Xie, C., Zhou, W., Du, W.,
1266 Li, J., Fu, P., Wang, Z., Worsnop, D. R., and Coe, H.: Changes in Aerosol Chemistry
1267 From 2014 to 2016 in Winter in Beijing: Insights From High-Resolution Aerosol Mass
1268 Spectrometry, *J. Geophys. Res.: Atmos.*, 124, 1132-1147,
1269 <https://doi.org/10.1029/2018jd029245>, 2019.

带格式的: 字体颜色: 超链接

带格式的: 字体颜色: 超链接

1270 Ye, Z., Liu, J., Gu, A., Feng, F., Liu, Y., Bi, C., Xu, J., Li, L., Chen, H., Chen, Y.,
1271 Dai, L., Zhou, Q., and Ge, X.: Chemical characterization of fine particulate matter in
1272 Changzhou, China, and source apportionment with offline aerosol mass spectrometry,
1273 *Atmos. Chem. Phys.*, 17, 2573-2592, <https://doi.org/10.5194/acp-17-2573-2017>, 2017.

带格式的: 字体颜色: 超链接

带格式的: 字体颜色: 超链接

1274 Yu, G., Zhang, Y., Yang, F., He, B., Zhang, C., Zou, Z., Yang, X., Li, N., and Chen,
1275 J.: Dynamic Ni/V Ratio in the Ship-Emitted Particles Driven by Multiphase Fuel Oil
1276 Regulations in Coastal China, *Environ. Sci. Technol.*, 55, 15031-15039,
1277 <https://doi.org/10.1021/acs.est.1c02612>, 2021.

带格式的: 字体颜色: 超链接

带格式的: 字体颜色: 超链接

1278 Yu, L., Smith, J., Laskin, A., Anastasio, C., Laskin, J., and Zhang, Q.: Chemical

1279 characterization of SOA formed from aqueous-phase reactions of phenols with the
1280 triplet excited state of carbonyl and hydroxyl radical, *Atmos. Chem. Phys.*, 14, 13801-
1281 13816, <https://doi.org/10.5194/acp-14-13801-2014>, 2014.

带格式的: 字体颜色: 超链接

带格式的: 字体颜色: 超链接

1282 Zhang, F., Wang, Y., Peng, J., Chen, L., Sun, Y., Duan, L., Ge, X., Li, Y., Zhao, J.,
1283 Liu, C., Zhang, X., Zhang, G., Pan, Y., Wang, Y., Zhang Annie, L., Ji, Y., Wang, G., Hu,
1284 M., Molina Mario, J., and Zhang, R.: An unexpected catalyst dominates formation and
1285 radiative forcing of regional haze, *Proc. Natl. Acad. Sci. U. S. A.*, 117, 3960-3966,
1286 <https://doi.org/10.1073/pnas.1919343117>, 2020.

带格式的: 字体颜色: 超链接

带格式的: 字体颜色: 超链接

1287 Zhang, G., Fu, Y., Peng, X., Sun, W., Shi, Z., Song, W., Hu, W., Chen, D., Lian,
1288 X., Li, L., Tang, M., Wang, X., and Bi, X.: Black Carbon Involved Photochemistry
1289 Enhances the Formation of Sulfate in the Ambient Atmosphere: Evidence From In Situ
1290 Individual Particle Investigation, *J. Geophys. Res.: Atmos.*, 126, e2021JD035226,
1291 <https://doi.org/10.1029/2021JD035226>, 2021.

带格式的: 字体颜色: 超链接

带格式的: 字体颜色: 超链接

1292 Zhang, Q., Canagaratna, M. R., Jayne, J. T., Worsnop, D. R., and Jimenez, J.-L.:
1293 Time- and size-resolved chemical composition of submicron particles in Pittsburgh:
1294 Implications for aerosol sources and processes, *J. Geophys. Res.*, 110,
1295 <https://doi.org/10.1029/2004JD004649>, 2005.

带格式的: 字体颜色: 超链接

带格式的: 字体颜色: 超链接

1296 Zhang, Q., Jimenez, J. L., Canagaratna, M. R., Ulbrich, I. M., Ng, N. L., Worsnop,
1297 D. R., and Sun, Y.: Understanding atmospheric organic aerosols via factor analysis of
1298 aerosol mass spectrometry: a review, *Anal. Bioanal. Chem.*, 401, 3045-3067,
1299 <https://doi.org/10.1007/s00216-011-5355-y>, 2011.

带格式的: 字体颜色: 超链接

带格式的: 字体颜色: 超链接

1300 Zhao, J., Qiu, Y., Zhou, W., Xu, W., Wang, J., Zhang, Y., Li, L., Xie, C., Wang, Q.,
1301 Du, W., Worsnop, D. R., Canagaratna, M. R., Zhou, L., Ge, X., Fu, P., Li, J., Wang, Z.,
1302 Donahue, N. M., and Sun, Y.: Organic Aerosol Processing During Winter Severe Haze
1303 Episodes in Beijing, *J. Geophys. Res.: Atmos.*, 124, 10248-10263,
1304 <https://doi.org/10.1029/2019jd030832>, 2019.

带格式的: 字体颜色: 超链接

带格式的: 字体颜色: 超链接

1305 Zhao, M., Zhang, Y., Ma, W., Fu, Q., Yang, X., Li, C., Zhou, B., Yu, Q., and Chen,
1306 L.: Characteristics and ship traffic source identification of air pollutants in China's
1307 largest port, *Atmos. Environ.*, 64, 277-286,
1308 <https://doi.org/10.1016/j.atmosenv.2012.10.007>, 2013.

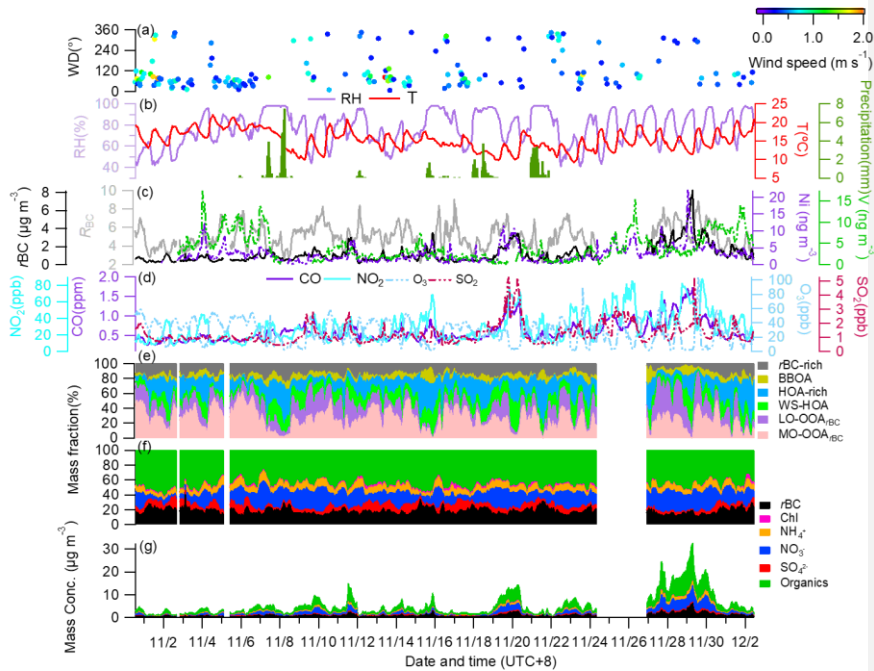
带格式的: 字体颜色: 超链接

带格式的: 字体颜色: 超链接

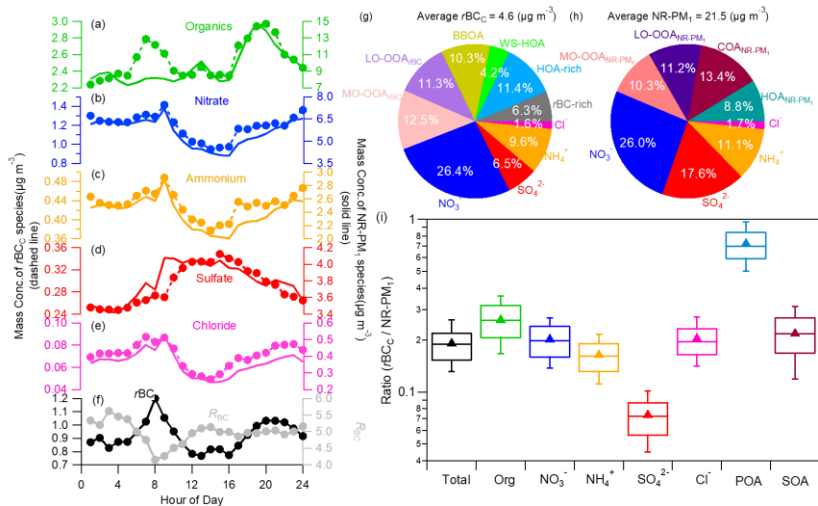
1309 Zhou, S., Collier, S., Xu, J., Mei, F., Wang, J., Lee, Y.-N., Sedlacek, A. J.,
1310 Springston, S. R., Sun, Y., and Zhang, Q.: Influences of upwind emission sources and
1311 atmospheric processing on aerosol chemistry and properties at a rural location in the
1312 Northeastern U.S, J. Geophys. Res.: Atmos., 121, 6049-6065,
1313 <https://doi.org/10.1002/2015jd024568>, 2016.
1314

带格式的: 字体颜色: 超链接

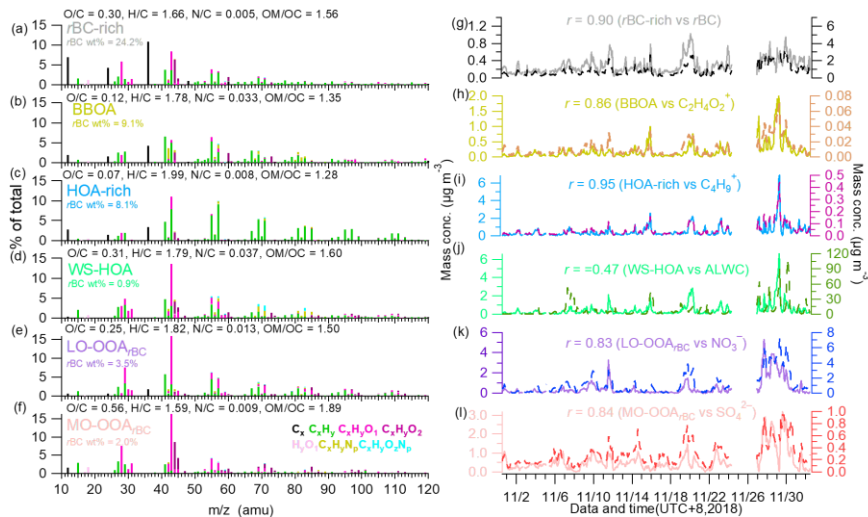
带格式的: 字体颜色: 超链接



1315
 1316 Figure 1. Time series of (a) wind direction (WD) colored by wind speed (WS), (b) air
 1317 temperature (T), relative humidity (RH) and precipitation, (c) mass concentrations of
 1318 *r*BC, Ni, V, and *R*_{BC} (mass ratio of all coating species to *r*BC), (d) mass concentrations
 1319 of gas pollutants of CO, NO₂, O₃ and SO₂, (e) mass fractions (%) of different OA factors
 1320 to the total *r*BCc OA, (f) mass fractions (%) of different components to the total *r*BCc
 1321 mass, and (g) mass concentrations of stacked *r*BCc components.



1322
 1323 Figure 2. Diurnal cycles of mass concentrations of (a–e) *r*BC_c and NR-PM₁ species
 1324 (organics, nitrate, ammonium, sulfate, and chloride), and (f) *r*BC and *R*_{BC}. Campaign-
 1325 average chemical composition of *r*BC_c (g) and NR-PM₁ (h). (i) Mass ratios of species
 1326 in *r*BC_c to those in NR-PM₁ (the whiskers above and below the boxes mark the 90%
 1327 and 10% percentiles, respectively; the upper and lower edge of the boxes represent the
 1328 75% and 25% percentiles, respectively; and the lines and triangles inside the boxes
 1329 denote the median and mean values, respectively; SOA represents $([LO-OOA_{rBC}] +$
 1330 $[MO-OOA_{rBC}])/([LO-OOA_{NR-PM1}] + [LV-OOA_{NR-PM1}])$, and POA represents $([rBC-rich$
 1331 $+ HOA-rich + BBOA + WS-HOA])/HOA_{NR-PM1}$).



1332

1333 Figure 3. High resolution mass spectra of (a) *r*BC-rich, (b) BBOA, (c) HOA-rich, (d)

1334 WS-HOA, (e) LO-OOA_{*r*BC}, and (f) MO-OOA_{*r*BC}. (g-l) Time series of corresponding

1335 factors, their tracers (*r*BC, C₂H₄O₂⁺, C₄H₉⁺, ALWC, nitrate and sulfate) as well as the

1336 correlation coefficients (ALWC refers to aerosol liquid water content, which was

1337 estimated by using the ~~extended aerosol inorganic model (Clegg et al., 1998).~~

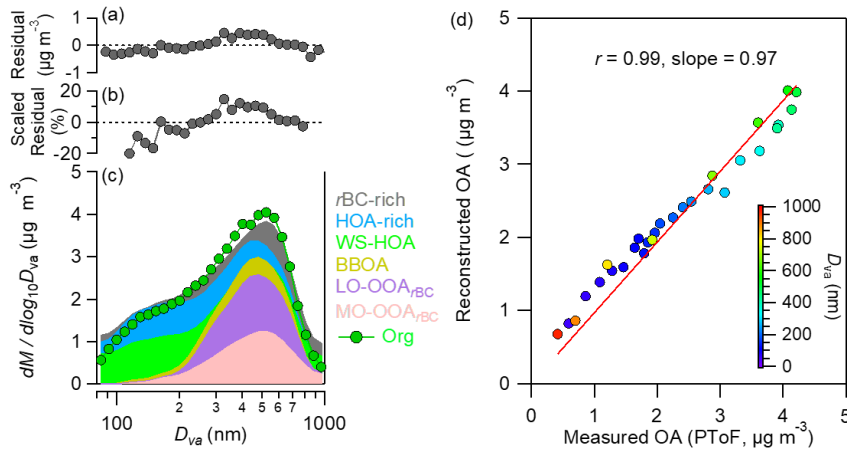
1338 ~~Calculated ALWC at different RH values is shown in Fig. S4model II of extended~~

1339 ~~aerosol inorganic model (E-AIM II)(Clegg et al., 1998); calculation details and results~~

1340 ~~at different RH values are described in the caption and shown in Fig. S5)~~

1341

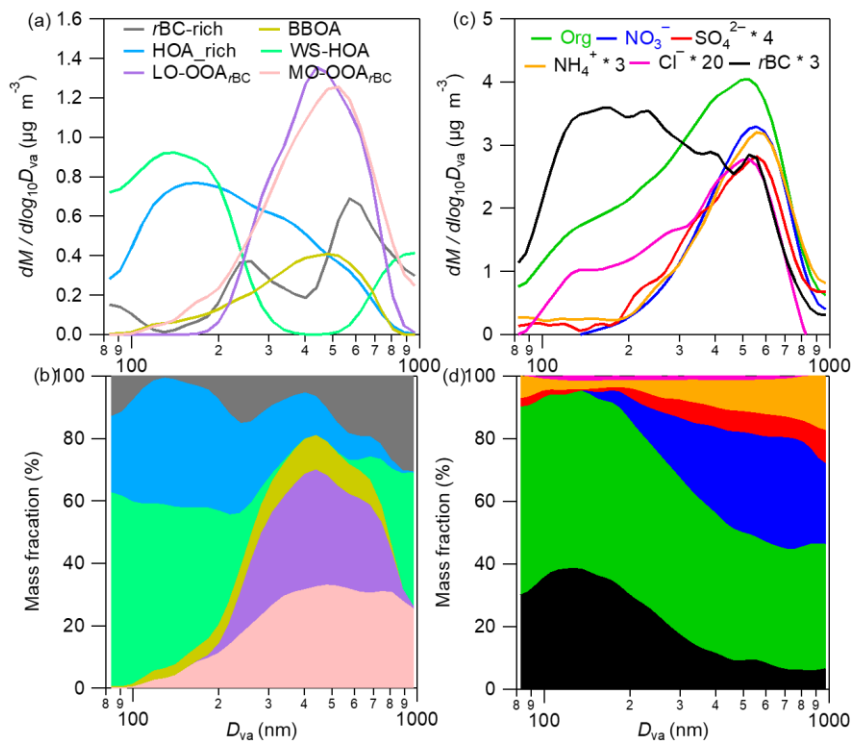
1342



1343

1344 Figure 4. Summary of key diagnostic plots of derivation of size distributions of
1345 individual *r*BCc OA factors. (a) Absolute and (b) relative residuals between the
1346 reconstructed and measured OA mass concentrations in different size bins. (c) Stacked
1347 size distributions of the six OA factors compared to the size distributions of total OA.
1348 (d) Reconstructed OA mass concentrations compared to the measured values for
1349 different size bins (80-1000 nm).

1350

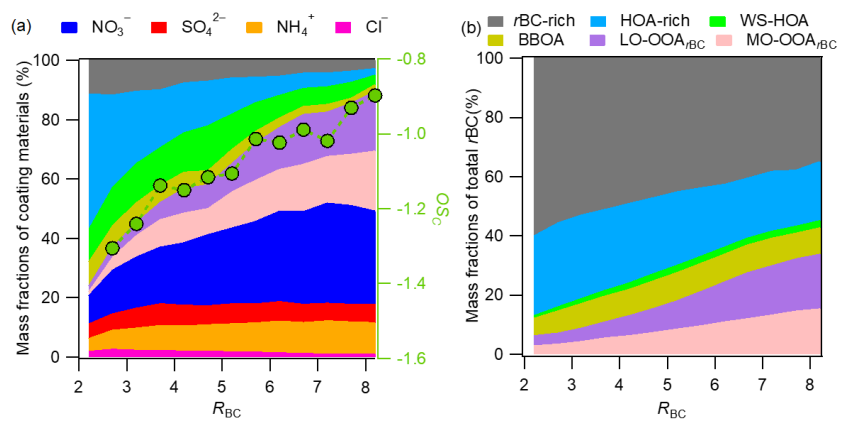


1351

1352 Figure 5. Campaign-average size distributions of six rBCc OA factors (a) and individual
 1353 rBCc components (b), and corresponding mass contributions of the six factors to the
 1354 total rBCc OA (c), and the major components to the total rBCc (d) at different sizes
 1355 (80-1000 nm).

1356

1357

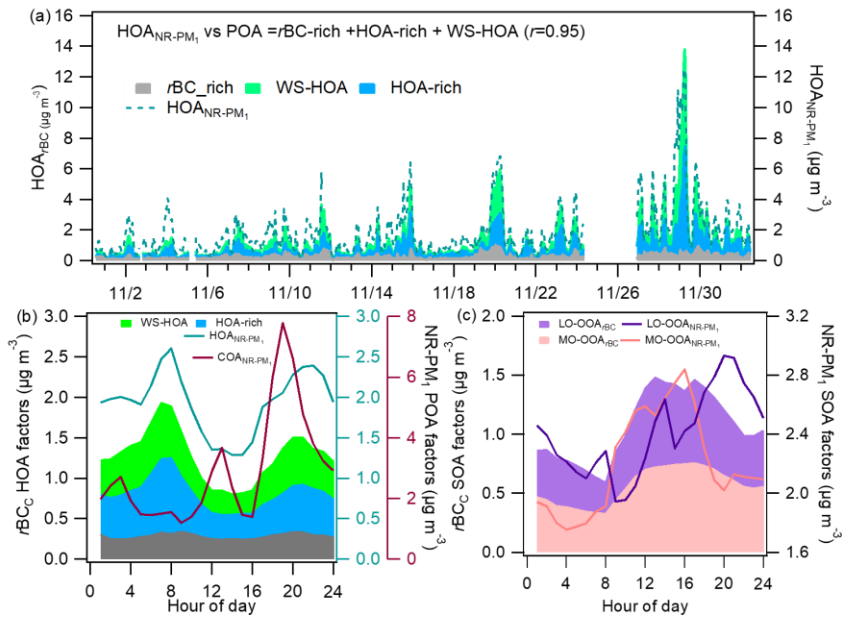


1358

1359 Figure 6. (a) Variations of mass fractions of the major $rBCc$ components against R_{BC} .

1360 (b) Variations of mass contributions of individual $rBCc$ OA factors to rBC against R_{BC} .

1361

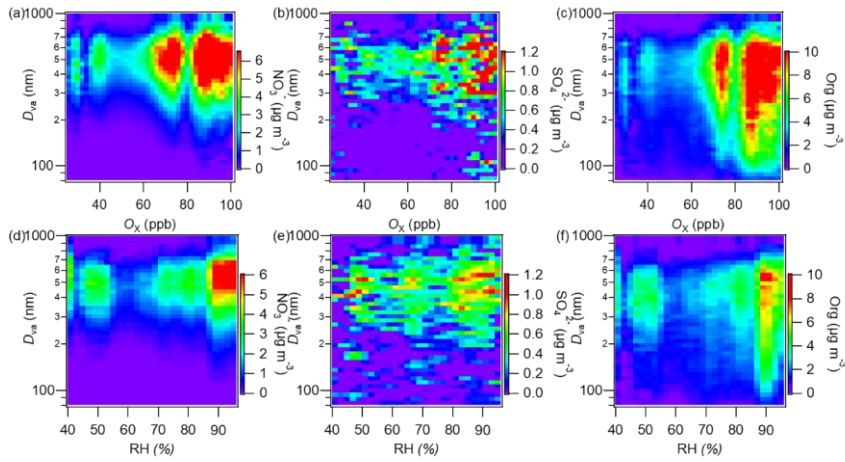


1362

1363 Figure 7. (a) Time series of stacked three rBC_c POA factors (i.e., rBC -rich, HOA-rich,
 1364 and WS-HOA) and HOA_{NR-PM1} . Comparisons of the diurnal patterns of different POA
 1365 factors (b) and SOA factors (c) of rBC_c and NR-PM₁.

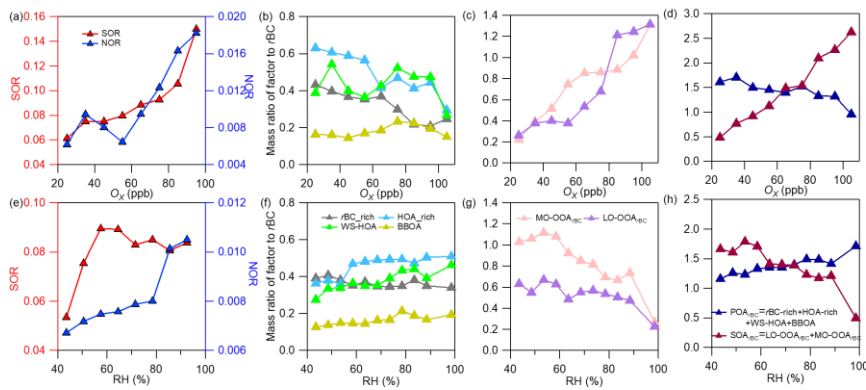
1366

1367



1368

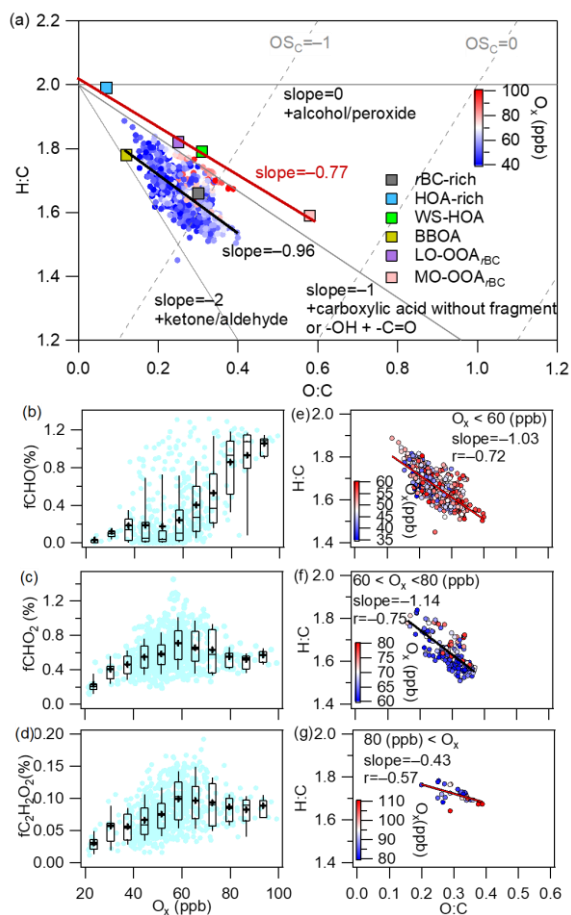
1369 Figure 8. Image plots of size distributions of rBCc nitrate, sulfate, organics as a function
1370 of (a-c) O_x and (d-f) RH, respectively (color represents its concentration).
1371



1372

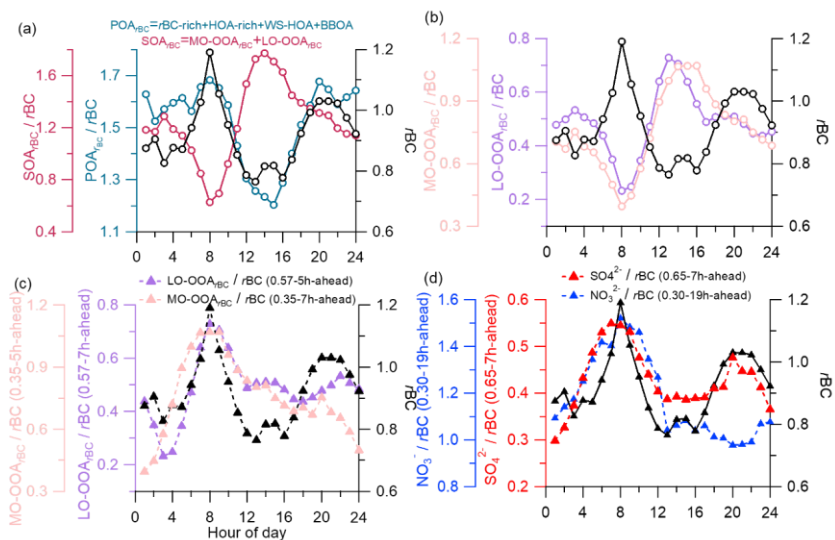
1373 Figure 9. Variations of nitrogen oxidation ratio (NOR) and sulfur oxidation ratio, mass
 1374 ratios of different POA factors, SOA factors and total POA and SOA to *rBC* against O_X
 1375 (a-d) and RH (e-h) ($NOR = nNO_3^- / (nNO_3^- + nNO_2 + nNO)$ and $SOR = nSO_4^{2-} / (nSO_4^{2-} + nSO_2)$,
 1376 where nNO_3^- , nSO_4^{2-} , nNO_2 , nNO and nSO_2 are the molar concentrations of particle-
 1377 phase sulfate, nitrate, gaseous NO_2 , NO and SO_2 , respectively).

1378

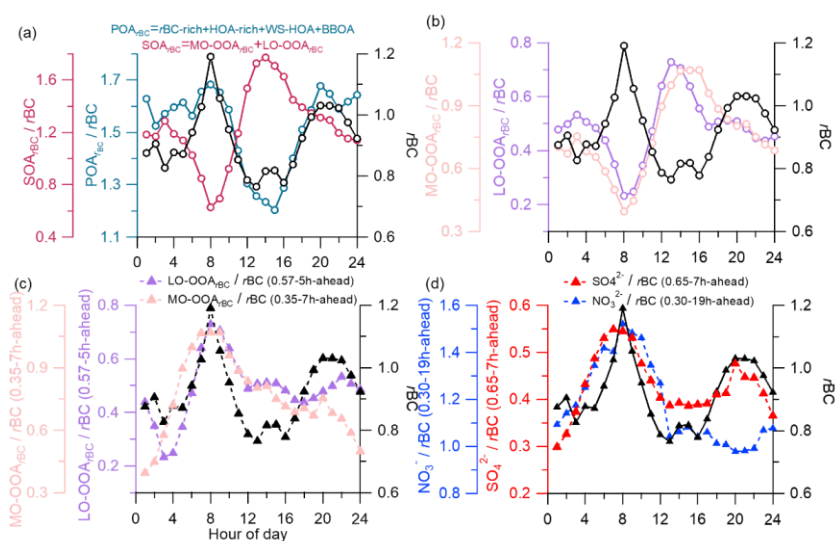


1379

1380 Figure 10. (a) Van Krevelen diagram of H/C versus O/C ratios for all rBCc OA and the
 1381 six factors colored by O_x concentrations (the black line represents the linearly fitted
 1382 line of all OA data, and the red line is the fitted line of the four OA factors). (b-d) Mass
 1383 fractions of selected oxygenated ion fragments as a function of O_x (meanings of the
 1384 boxes are the same as those described in Fig. 2). (e-g) Scatter plots of H/C versus O/C
 1385 ratios under different O_x levels (data are colored by O_x concentrations).



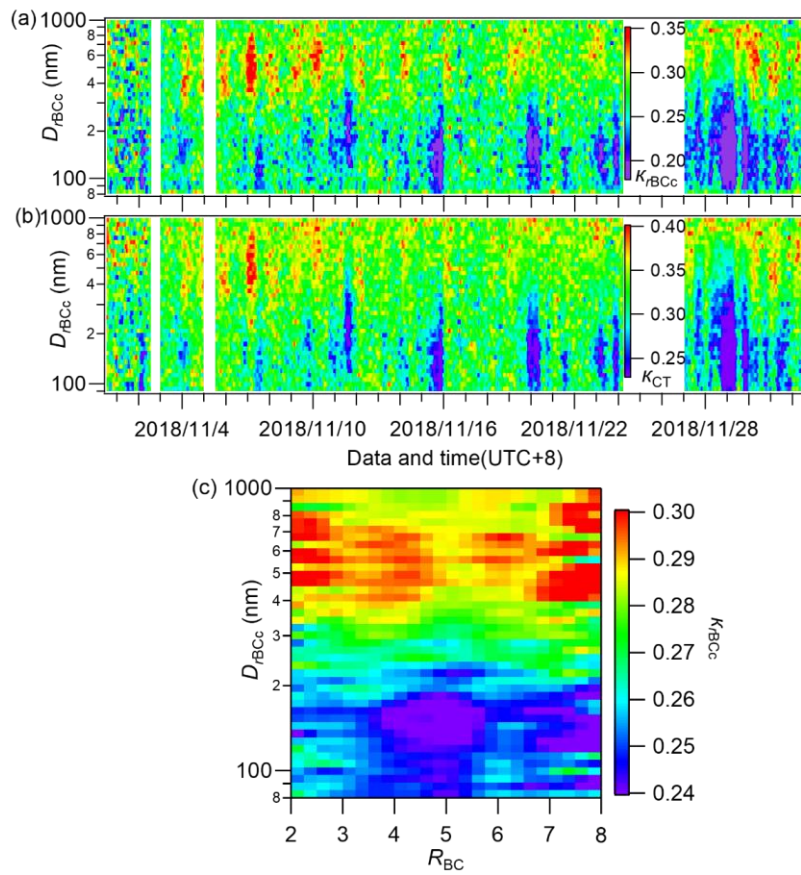
1386



1387

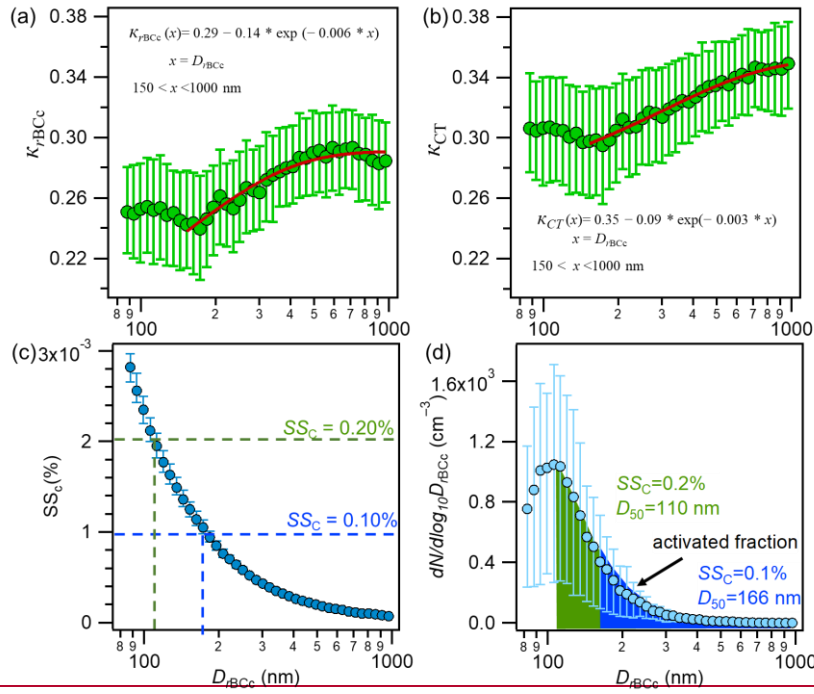
1388 Figure 11. Campaign-average diurnal patterns of (a) rBC , POA_{rBC}/rBC and
 1389 SOA_{rBC}/rBC , and (b) rBC , $MO-OOA_{rBC}/rBC$ and $LO-OOA_{rBC}/rBC$. Adjusted diurnal
 1390 patterns by the average coating time (ACT) for (c) $LO-OOA_{rBC}/rBC$, $MO-OOA_{rBC}/rBC$,
 1391 and (d) SO_4^{2-}/rBC , NO_3/rBC .

1392

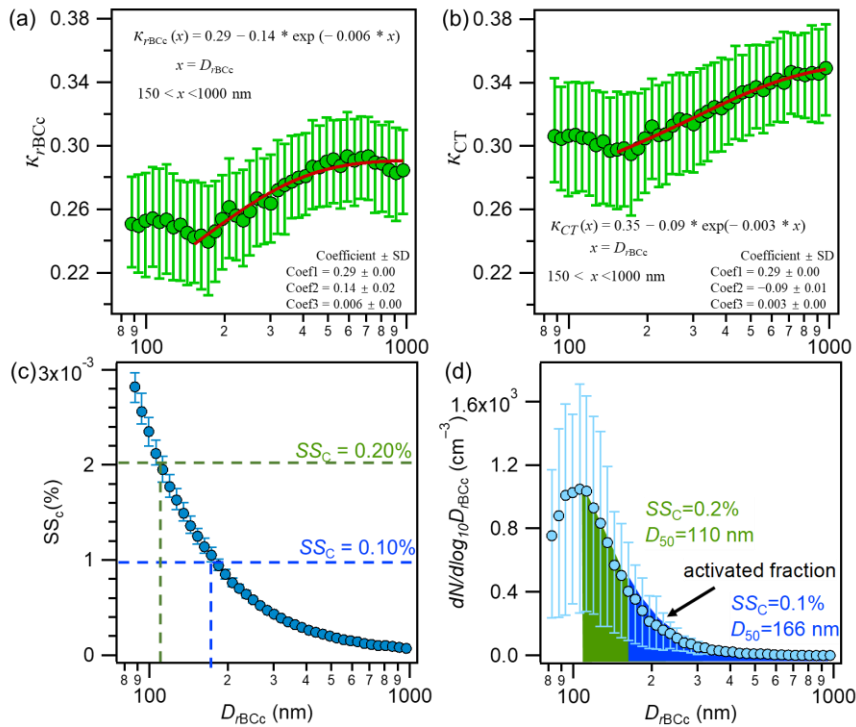


1393

1394 Figure 12. Image plots of size-resolved hygroscopicity parameters of (a) $rBCc$ (κ_{rBCc}),
 1395 (b) its coating materials (κ_{CT}) during the whole campaign, and (c) the campaign-average
 1396 size-resolved κ_{rBCc} at different R_{BC} .

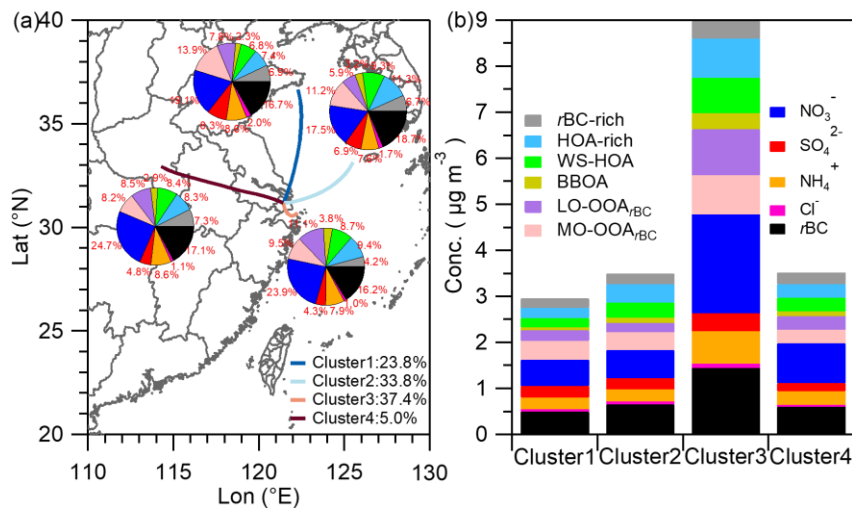


1397



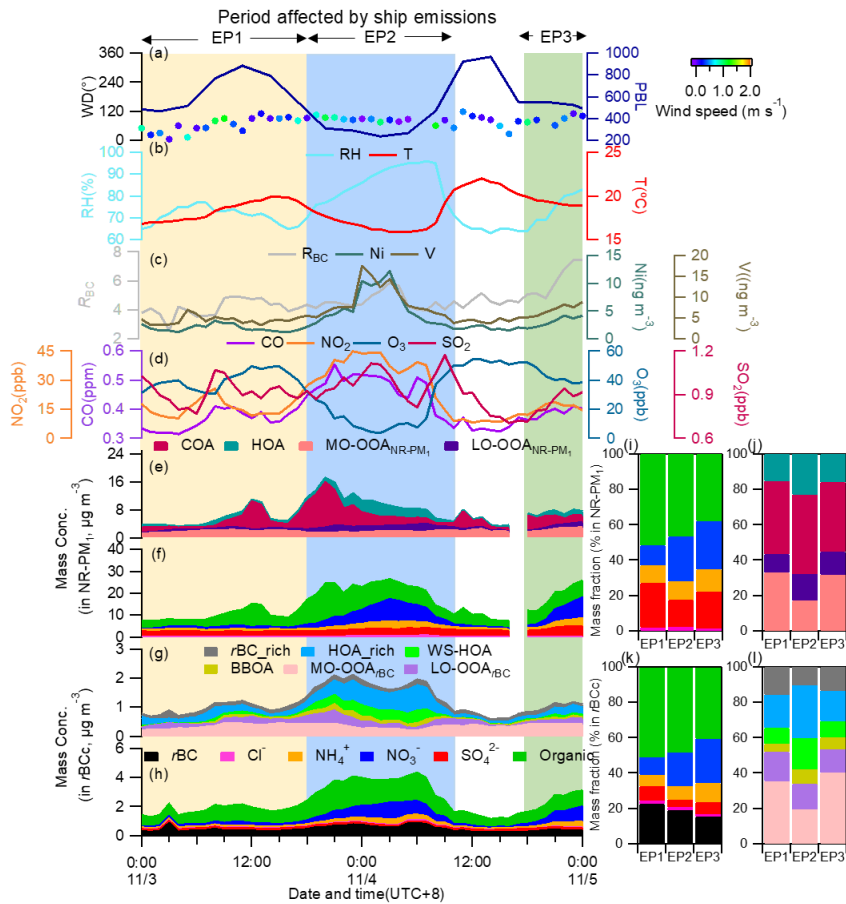
1398

1399 Figure 13. Campaign-average size-resolved hygroscopic parameters for $rBCc$ (κ_{rBCc})
 1400 and (a) for its coatings (κ_{CT}) (b) (the red lines are exponential fits of the data of 150-
 1401 1000 nm). (c) Campaign-average size-resolved critical supersaturation (SS_c), and (d)
 1402 the predicted activated fraction of $rBCc$ number concentration based on D_{50} at SS_c of
 1403 0.1% (166 nm) and 0.2% (110 nm) (the solid circles are mean values, the upper and
 1404 lower lines are the 75th and 25th percentiles, respectively).



1405

1406 Figure 14. (a) Four clusters of 24-h backward trajectories (at altitude of 500 m) analyzed
 1407 by NOAA HYSPLIT model (<http://www.arl.noaa.gov/ready/hysplit4.html>) embedded
 1408 in Zefir (Petit et al., 2017) (Petit et al., 2017), with the pie chart showing the average
 1409 rBC_c chemical compositions in each cluster. (b) Stacked mass concentrations of the
 1410 rBC_c components of the four clusters.



1411
 1412 Figure 15. Time series of (a) wind direction (WD) colored by wind speed (WS),
 1413 planetary boundary layer (PBL) height, (b) relative humidity (RH) and temperature (T),
 1414 (c) mass concentrations of particle-phase Ni and V, and R_{BC} , (d) mass concentrations of
 1415 CO, NO₂, O₃, SO₂, stacked concentrations of (e) NR-PM₁ OA factors, (f) NR-PM₁
 1416 species, (g) $rBCc$ OA factors, and (h) $rBCc$ components during the ship emission period
 1417 (SEP). Mass contributions of different components to NR-PM₁ (i), different OA factors
 1418 to total NR-PM₁ OA (j), different components to $rBCc$ (k), and different OA factors to
 1419 total $rBCc$ OA (l) for the three episodes (EP1, EP2 and EP3).
 1420